

Article

Numerical Investigation of the Secondary Swirling in Supersonic Flows of Various Nature Gases

Vyacheslav Volov ^{1,*}, Nikolay Elisov ²  and Anton Lyaskin ³¹ Natural Science Department, Samara State Transport University, 443066 Samara, Russia² Independent Researcher, 443086 Samara, Russia; mr07th@gmail.com³ Department of Expertise, "ERA" Military Innovative Technopolis, 353456 Anapa, Russia; alyaskin@gmail.com

* Correspondence: volovvt@mail.ru; Tel.: +7-960-831-99-34

Abstract: Despite the application of vortex tubes for cooling, separating gas mixtures, vacuuming, etc., the mechanism of energy separation in vortex tubes remains an object of discussion. This paper studies the effect of secondary swirling in supersonic flows on the energy separation of monatomic and diatomic gases. The approach used is a numerical solution of the Reynolds-averaged Navier-Stokes equations, closed by the Reynolds Stress Model turbulence model. The modelling provided is for a self-vacuuming vortex tube with air, helium, argon, and carbon dioxide. According to the results of the calculations, the effect of secondary swirling is inherent only in viscous gases. A comparison was made between obtained total temperature difference, the level of secondary swirling and power losses on expansion from the nozzle, compression shocks, friction, turbulence, and energy costs to develop cascaded swirl structures. Our results indicate that helium and argon have the highest swirling degree and, consequently, the highest energy separation. Moreover, it can be concluded that the power costs on the development of cascaded vortex structures have a significant role in the efficiency of energy separation.



Citation: Volov, V.; Elisov, N.; Lyaskin, A. Numerical Investigation of the Secondary Swirling in Supersonic Flows of Various Nature Gases. *Energies* **2021**, *14*, 8122. <https://doi.org/10.3390/en14238122>

Academic Editor: Irina G. Akhmetova

Received: 1 November 2021

Accepted: 25 November 2021

Published: 3 December 2021

Publisher's Note: MDPI stays neutral with regard to jurisdictional claims in published maps and institutional affiliations.



Copyright: © 2021 by the authors. Licensee MDPI, Basel, Switzerland. This article is an open access article distributed under the terms and conditions of the Creative Commons Attribution (CC BY) license (<https://creativecommons.org/licenses/by/4.0/>).

Keywords: Ranque-Hilsch vortex tube; energy separation; tangential nozzle; computational fluid dynamics

1. Introduction

The vortex tube was first invented in 1933 by Georges Ranque [1]. The phenomenon of energy separation (Ranque effect) is separated into two streams: hot and cold. In 1947 Rudolph Hilsch proposed a recommendation while developing these devices [2], and vortex tubes became known as Ranque-Hilsch vortex tubes. Further experimental studies showed that the axial and radial velocity components were much smaller than tangential [3]. It was also established that the static temperature decreased in a radial direction. Fulton [4] discussed the energy separation resulting from the flow separation into two streams: a high angular velocity near the axis and a low angular velocity at the periphery. Similar conclusions were obtained independently by Van Deemter [5] and suggested that the difference between the performance of the vortex tube and Fulton's relations related to the incorrect assessment of the turbulent heat flux. Deissler and Perlmutter [6] concluded that the turbulent viscosity has larger order compared to the molecular velocity. Moreover, it was established that the working fluid must be compressible because the total temperature in an incompressible vortex can only increase. In 1961, Reynolds [7] proposed one of the widely favoured explanations of the Ranque effect. It estimates that the flow in the vortex tube slowly changes from a free to a forced vortex and the presence of a strong radial pressure gradient leads to a temperature profile, which almost complies with the adiabatic temperature distribution. However, another series of experiments [8,9] showed that the low value of cold mass fraction contradicts this hypothesis. Therefore, the hypothesis of vortices interaction was suggested, which removed this contradiction [10,11]. Additional research [10] presented the experimental test results of the hypothesis of vortices interaction.

The test provided for an SVT with two diffusers where the temperature decreased by 150 °C. According to this hypothesis, the micro-refrigeration cycles carry out the energy separation due to the turbulent moles [12].

Currently, vortex tubes are applied for cooling where small dimensions are required, i.e., separating gas mixtures, vacuuming, etc. However, it has a lower efficiency in comparison to traditional refrigeration systems in the industry. Despite this, many researchers continue to study vortex tubes for various applications. Several papers [13,14] present the investigation results of a vortex tube used on the cold start of a diesel engine at various ambient temperatures for exhaust emission characteristics. One of the main conclusions is that vortex tubes have reduced fuel consumption and CO emissions, but NO emission has increased. Other research [15] suggested using a vortex tube for cooling the hydrogen fueling station. As the authors noted, using a vortex tube decreases electricity and production costs which simplifies construction and achieves fast cooling. Additional research [16] showed that applying a vortex tube in a waste heat recovery system decreases energy costs. Shmroukh et al. [17] proposed using a vortex tube for seawater desalination. An optimum system vacuum pressure and operation mode was established to provide a high amount of desalinated water after a series of experiments. Moreover, the authors [18] noted that vortex tubes could be applied to the problems related to a trans-critical CO₂ refrigeration system, gas dehydration, and dew point control. Additionally, Nash [19] considered the application of vortex tubes in a spacecraft's environmental control system.

Other studies have focused on optimizing the vortex tube design. For example, researchers [20] investigated the influence of vortex chamber form on the vortex tube performance. Additional research [21] presented the shape optimization results of a hot control valve in a vortex tube. The best performance was established with a truncated cone control valve as compared to the spherical plate and cone forms. Guo and Zhang [22] suggested vortex tube optimization criteria based on the vortex structure analysis. The authors concluded that optimum flow could be achieved with the maximum possible extension of the central reverse region and increasing the precessing vortices number by covering the whole tube. Further research [23] presents experimental series results obtained at various inlet pressures, nozzle numbers, cold cone angles, and wall materials. Additional researchers [24] considered vortex tubes with helical nozzles on energy separation. They provided a series of numerical experiments with various nozzle numbers and radial distances. As results showed, the vortex tube with three helical nozzles had the best performance as compared to others. Another experiment [25] established that vortex tubes with lower aspect ratios perform better than larger nozzle aspect ratios. This effect was explained by the backflow mechanism that occurs near the cold exit. The paper [26] suggests installing the navigator angle into a vortex tube, which has improved cooling performance. Additional research [27] presented results obtained for different sizes of cold orifice ratio and hot exit areas, different metrics, and different working conditions. Based on obtained results, the authors suggested an optimization method for further studies of vortex tubes performance.

Additionally, part of the research related to a vortex tube is devoted to studying energy separation processes that occur within it. For example, Xue et al. [28] proposed that temperature separation is carried out by the temperature drop at the cold end and temperature rise at the hot end. The paper [29] focuses on investigating energy separation characteristics of CO₂-CH₄ binary gas inside a vortex tube. The authors established that pure CH₄ has the best performance in comparison with CO₂. The modelling of a mixture of CO₂-CH₄ also showed that CH₄ has larger magnitudes of temperature separation than CO₂. Aghagoli and Sorin [30] presented the study results for the vortex tube with CO₂ using a real gas model. Further research [31] provided a numerical analysis of the energy separation performance in vortex tubes with gaseous hydrogen for a wide temperature range. One of the main conclusions was the significant decrease in cooling power due to the decrease in inlet temperature. Other research [32] presented numerical results for self-vacuuming tubes (SVT) with helium. Obtained results showed that main power losses occur

due to shocks and secondary swirl generation. Another paper [33] showed that a vortex tube with three inlet nozzles has the most significant secondary and tertiary structures and excellent cooling performance. In addition, ref. [33] presented the good agreement between numerical results obtained using the Reynolds-average Navier-Stokes equation and Reynolds Stress Model (RSM) Omega turbulence model with the experimental data. Vitovsky [34] presented experiment results of the influence of inlet and outlet pressures on temperature separation. It was found that an increase in inlet pressure led to an increase in flow temperature separation. On the other hand, increasing outlet pressure leads to a decrease in flow temperature separation. Similar results were obtained in additional research as well [35]. Aside from this, it was found that a tapering angle of more than 4 degrees leads to decreased energy separation. The papers [36,37] estimated the precessing frequency of the energy separation by laser Doppler velocimetry. Results showed that the decrease in the precession characteristics leads to the decrease of the energy separation performance. In addition, the authors established that the increase in inlet pressure leads to an increase in vortex tube performance. Another paper [38] presented the results of a series of numerical simulations to analyze the effect of different external conditions on the flow structure. Based on the vortex breakdown theory, it was concluded that the axial pressure gradient significantly affects the vortex structure. Kirmaci et al. [39,40] studied the effect of the nozzle wall material on the performance of a vortex tube. They found that steel and aluminium have the best results in comparison with fibreglass.

SVT presents a special type of vortex tubes with one gas outlet through the diffuser (Figure 1). Compressed gas passes to the tangential nozzles, where the flow accelerates and enters the vortex camera and twists intensely. In addition, it was revealed that the turbulent viscosity is several orders of magnitude higher than the molecular viscosity and the heat transfer coefficient λ reaches the values of 10^2 to 10^3 W/m² [11]. This result makes it possible to use SVT as an effective cooling device for cooling bodies of axial symmetry placed in its axial region.

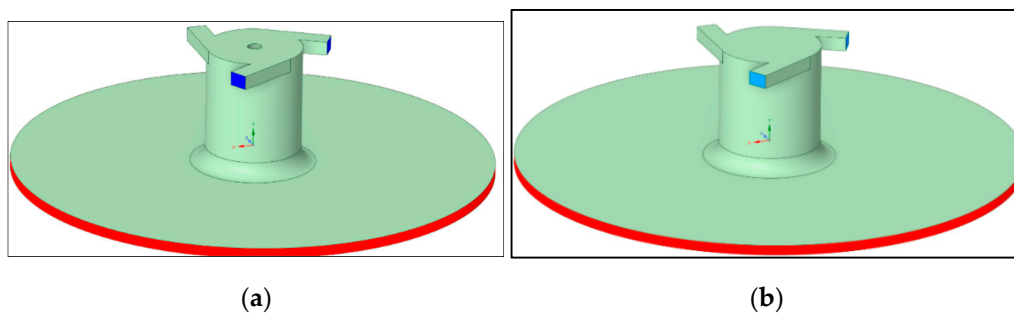


Figure 1. Model of investigated SVT (a) with the inner body (case 1) and (b) without the inner body (case 2).

This paper continues in these investigations [33,34] and raises the question of studying nature gases' influence on the energy separation in SVT. The problem was addressed for air, He, Ar, and CO₂ for different SVT.

2. Materials and Methods

2.1. Flow Equations

One of the ways to describe the motion of a compressible flow is the RANS equation, supplemented by the energy equation:

$$\frac{\partial \rho}{\partial t} + \frac{\partial}{\partial x_i}(\rho u_i) = 0, \quad (1)$$

$$\frac{\partial}{\partial t}(\rho u_i) + \frac{\partial}{\partial x_j}(\rho u_i u_j) = \frac{\partial p}{\partial x_i} + \frac{\partial}{\partial x_j} \mu \left(\frac{\partial u_i}{\partial x_j} + \frac{\partial u_j}{\partial x_i} - \frac{2}{3} \delta_{ij} \frac{\partial u_k}{\partial x_k} \right) + \frac{\partial}{\partial x_j} (-\rho \overline{u'_i u'_j}), \quad (2)$$

$$\frac{\partial}{\partial t}(\rho E) + \frac{\partial}{\partial x_i}[u_i(\rho E + p)] = \frac{\partial}{\partial x_j} \left[k_{eff} \frac{\partial T}{\partial x_j} + u_i(\tau_{ij})_{eff} \right]. \quad (3)$$

where ρ is density, u is the average fluid velocity, p is pressure, μ is dynamic viscosity, δ_{ij} is Kronecker delta, $(-\rho \overline{u'_i u'_j})$ is Reynolds stress, E is total energy, k_{eff} is effective thermal conductivity, and T is temperature, $(\tau_{ij})_{eff}$.

Effective thermal conductivity k_{eff} and effective shear stress $(\tau_{ij})_{eff}$ are defined by the relations:

$$k_{eff} = k + k_\tau, \quad (4)$$

$$k_\tau = c_p \frac{\mu_\tau}{Pr_\tau}, \quad (5)$$

$$(\tau_{ij})_{eff} = \mu_{eff} \left(\frac{\partial u_j}{\partial x_i} + \frac{\partial u_i}{\partial x_j} \right) - \frac{2}{3} \mu_{eff} \frac{\partial u_k}{\partial x_k} \delta_{i,j}, \quad (6)$$

$$\mu_{eff} = \mu + \mu_\tau, \quad (7)$$

$$\mu_\tau = \rho C_\mu \frac{TKE^2}{\varepsilon}, \quad (8)$$

where k is thermal conductivity, k_τ is turbulent thermal conductivity, μ_τ is turbulent dynamic viscosity, Pr_τ is turbulent Prandtl number, μ_{eff} is effective dynamic viscosity, C_μ is a constant that equals 0.09, TKE is turbulence kinetic energy, and ε is the rate of dissipation of TKE .

The turbulent Prandtl number assumes the constant and is equal to 0.85. To solve RANS equations, they must be closed by one of the turbulence models. The solution of RANS equations is conducted in two stages. The first stage is the solution by the $k-\omega$ SST turbulence model [41] to form the main flow. The second stage is the calculation by the RSM Omega [42] to clarify the obtained results.

This clarification is based on the following point. Usually, SVT have small sizes, leading to the low value of the parameter of y_+ . RSM Omega does not require viscous damping functions to resolve the near-wall sublayer [43]. Additionally, this model shows itself as a more robust and universal model in the class of two-equation models. When using the RSM Omega, Equation (8) will be rewritten in the following form:

$$\mu_\tau = \rho \frac{TKE}{\omega}, \quad (9)$$

where ω is the specific dissipation rate.

2.2. Power Costs and Losses Estimation Inside SVT

Based on the limit energy theory [44], we can obtain maximum power, which goes to the utilization (some beneficial effect) and losses inside SVT [40]:

$$\Delta N = \Delta \bar{N} c_p T_{in}^* G, \quad (10)$$

$$\Delta \bar{N} = \frac{1}{\gamma} \frac{\gamma - 1}{\gamma + 1} (\lambda_1^2 - \lambda_{out}^2), \quad (11)$$

$$\lambda = M \sqrt{\frac{\gamma + 1}{2[1 + 0.5(\gamma - 1)]}} M^2, \quad (12)$$

where c_p is specific heat capacity, T_{in}^* is the total temperature at the inlet, G is mass flow rate, γ is heat capacity ratio, M is Mach number, and $\Delta \bar{N}$ is the maximum value of lost or utilized flow power fraction into the vortex tube [44].

In turn, the maximum possible power losses can be grouped into losses on the friction N_{visc} , turbulence N_τ , expansion from nozzles N_{en} , compression shocks N_{cs} , and cost to

develop the cascaded swirl structures N_{sw} . The following relation estimates the power losses on the friction N_{visc} :

$$N_{visc} = \int |\tau| V_{dyn} ds, \quad (13)$$

$$V_{dyn} = \sqrt{\frac{|\tau|}{\rho}}, \quad (14)$$

where V_{dyn} is dynamic velocity.

$$N_{\tau} = \int \frac{TKE\rho}{t_{av}} dV, \quad (15)$$

where t_{av} is the average time of flow through SVT.

Power losses on the expansion from nozzles N_n is defined as:

$$N_n = \left(1 - \frac{S_n}{S_t}\right) \frac{G_1(v_1 - v_2)^2}{2}, \quad (16)$$

where S_n is nozzle area, S_t is tube area, v_1 is velocity before expansion, and v_2 is velocity after expansion.

The assessment of power losses on the compression shocks can be done through the shock wave theory following Abramovich [45]. Finally, power costs on the development of cascaded swirl structures can be defined as the difference between the maximum possible power loss and costs to some beneficial effect and its components:

$$N_{sw} = \Delta N - N_{visc} - N_{\tau} - N_{cs}. \quad (17)$$

Also, power costs on the development of cascaded swirl structures may be calculated by the relation presented in the paper [33]:

$$N_{sw} = \frac{GV_{\theta}^2}{2}, \quad (18)$$

where V_{θ} is secondary swirling velocity.

2.3. Problem Formulation

Our research considers the SVT presented in Figure 1. To achieve the best cooling, SVT should have three rectangle nozzles with an aspect ratio of 3:2, and a ratio of the nozzle area to the vortex tube of 0.08. In Figure 1, the blue colour is the inlet, and the red colour is the outlet.

The considered SVT has geometric parameters presented in Figure 2.

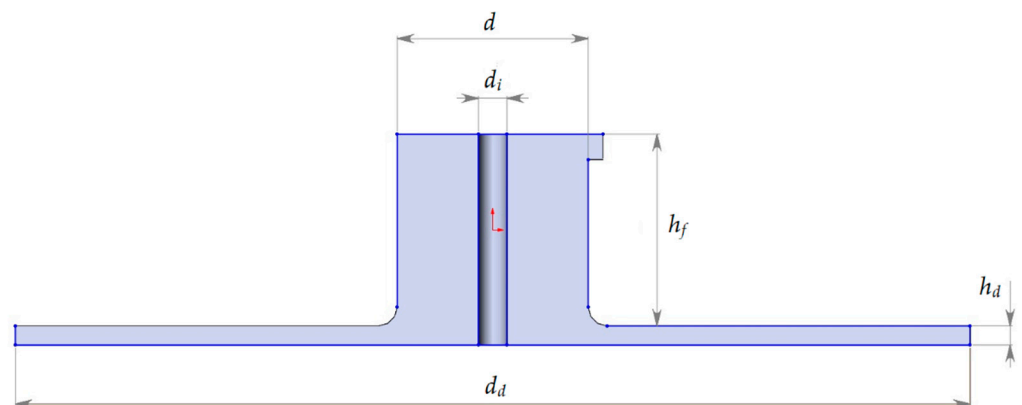


Figure 2. SVT geometric parameters.

It should be noted that *He*, *Ar*, *CO₂*, and air have different thermodynamic properties and have different Reynolds numbers for one SVT geometry (Table 1). Thus, it is also necessary to model SVT for a similar Reynolds number to assess its effect on the performance.

Table 1. Reynolds number of gases.

Gas	Reynolds Number
<i>He</i>	81,518
<i>Ar</i>	293,785
<i>CO₂</i>	188,425
<i>Air</i>	280,917

As seen from Table 1, *Ar* has the highest Reynolds number. Therefore, one of the ways to increase the Reynolds number for *He*, *CO₂*, and air to the values obtained for *Ar* is by increasing the tube diameter *d*. Calculation of the required diameter is carried out by the following relations:

$$d = \frac{Re_{Ar} \nu}{a}, \quad (19)$$

$$a = \sqrt{\gamma RT}, \quad (20)$$

where Re_{Ar} is the Reynolds number obtained for *Ar*, ν is the kinematic viscosity, a is local sound speed, and R is the gas constant.

SVT geometric parameters provide the same Reynolds number given in Table 2.

Table 2. Geometric parameters of investigated SVT.

Gas	Tube Diameter <i>d</i> , mm	Nozzle Length <i>l_n</i> , mm	Nozzle Height <i>h_n</i> , mm	Diffuser Diameter <i>d_d</i> , mm	Diffuser Height <i>h_d</i> , mm
<i>Ar</i>	10	1.98	1.32	50	1
<i>He</i>	36	7.14	4.76	180	1.05
<i>CO₂</i>	15.6	2.95	1.96	78	1.56
<i>Air</i>	10.5	2.08	1.38	52.5	3.6

The inner body has a diameter d_i equal to 15% of tube diameter d . All considered SVTs have a length h_f of 10 mm. This was chosen to be constant since a decrease in the tube length of less than one calibre has an insignificant effect on energy separation.

2.4. Numerical Approaches

The 3D mesh of the studied SVT is presented in Figure 3. The polyhedral grid is used to provide more precise calculations. The modelling was conducted using ANSYS Fluent.

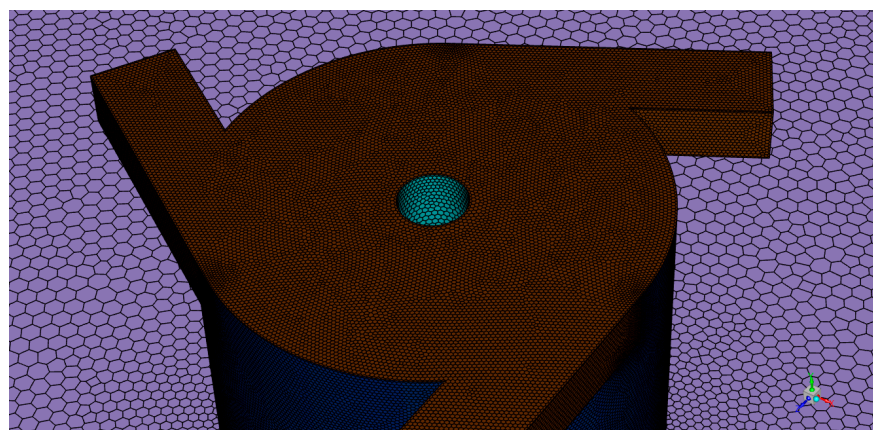


Figure 3. Surface mesh.

Previous papers [33,34] devoted to this study used the commercial CFD package ANSYS CFX. As is known, ANSYS CFX is based on the pressure-based solver. According to the presented methodology [32], this paper also uses a pressure-based solver to solve the problems.

Since the research considers the thermodynamic problem, the coupled scheme was chosen for its correct solution when using a pressure-based solver. The second-order spatial discretization was used while $k-\omega$ SST was used. The first order of the discretization scheme for the Reynolds stresses dissipation rate and momentum used the RSM Omega model. This is because the compressible flow and the RSM Omega model combination significantly decreased the solution stability when using a pressure-based solver. The pseudo-transient method was used with the pseudo-step $\Delta t = 10^{-6}$ s for the $k-\omega$ SST model and $\Delta t = 10^{-7}$ s for the RSM Omega model.

All considered gases are calculated according to the perfect gas model. Such parameters as specific heat c_p , thermal conductivity λ , and dynamic viscosity μ are defined following Perry's handbook [46].

The modelling of considered SVT provided for the following conditions presented in Table 3.

Table 3. Modelling conditions.

Boundary Condition	Pressure p , atm	Temperature T , K
Inlet	3	500
Outlet	1	300

Boundary conditions for walls are smooth adiabatic walls both for the outer side and inner body.

2.5. Mesh Independence Study

The classical approach to analyzing mesh independence, implying a double increase of the grid element number [47], can lead to significant computational costs for three-dimensional problems. Thus, it is most practical to provide a mesh independence study with a non-uniform increase in the grid element number. The mesh independence study with a non-uniform increase in elements number is provided in following the paper [48]:

$$P = \frac{\left| \ln \left(\frac{|f_3 - f_2|}{f_2 - f_1} \right) + q(p) \right|}{\ln r_{21}}, \quad (21)$$

$$q(p) = \ln \left(\frac{r_{21}^P - s}{r_{32}^P - s} \right), \quad (22)$$

$$s = \text{sign} \left(\frac{f_3 - f_2}{f_2 - f_1} \right), \quad (23)$$

where P is convergence order, f_i is grid solutions, and r_{ij} is the mesh refinement ratio defined as:

$$r_{ij} = \frac{h_i}{h_j}, \quad (24)$$

Here, h_i is a number of grid elements. The transcendental Equation (21) is solved with the initial condition $q(p) = 0$ until the solution converges. The grid convergence index (GCI) is estimated to assess the discretization error. For a non-uniform grid refinement ratio, it has the following view:

$$GCI_{21} = F_s \frac{\varepsilon_{21}}{r_{21}^P - 1}, \quad (25)$$

$$GCI_{32} = F_s \frac{\varepsilon_{32}}{r_{32}^p - 1}, \quad (26)$$

where F_s is the safety factor and is equal to 1.25 and ε_{ij} is relative error defined as:

$$\varepsilon_{ij} = \frac{f_i - f_j}{f_i}. \quad (27)$$

In this paper, the parameter f is the maximum decreasing of total temperature T .

A mesh independence study was conducted for all considered gases and SVTs, i.e., for the same geometry, for the Reynolds numbers, and the same Reynolds number without the inner body. The grid sizes are presented in Table 4 for SVT with the same Reynolds number.

Table 4. Grid independence analysis for SVT with the same Reynolds number.

Gas	Elements Number for Case No. 1	Elements Number for Case No. 2	Elements Number for Case No. 3
Ar	2,825,328	3,932,631	6,028,786
He	5,291,541	7,078,257	9,568,966
CO ₂	3,724,078	5,128,536	7,542,893
Air	2,969,191	4,206,553	6,572,770

The mesh sizes are shown in Table 5 for SVT with the same Reynolds number and without the inner body.

Table 5. Grid independence analysis for SVT with the same Reynolds number without the inner body.

Gas	Elements Number for Case No. 1	Elements Number for Case No. 2	Elements Number for Case No. 3
Ar	2,695,33	3,8203,92	5,957,826
He	5,259,305	6,891,704	9,360,088
CO ₂	3,6697,40	5,068,259	6,899,789
Air	2,851,452	4,102,444	6,513,116

3. Results and Discussions

Calculations were carried out using a Samara University supercomputer “Sergey Korolev”. The calculations were provided for cases of inviscid gases, SVT with the same geometry, SVT with the same Reynolds number, and SVT with the same Reynolds number without the inner body. All calculations were conducted using double precision.

3.1. Case of Inviscid Gases

Modelling the inviscid gas in SVT with Ar, CO₂, and air showed a similar result (Figure 3) obtained in previous research [22]. As shown in Figure 4, streamlines move along the outer wall to the outlet.

The total temperature contour drawn along the nozzles shows that the absence of gas viscosity leads to SVT with no cooling efficiency (Figure 5).

Thus, we can conclude that the formation of secondary swirls occurs due to viscosity. Additionally, the absence of viscosity leads to no energy separation processes.

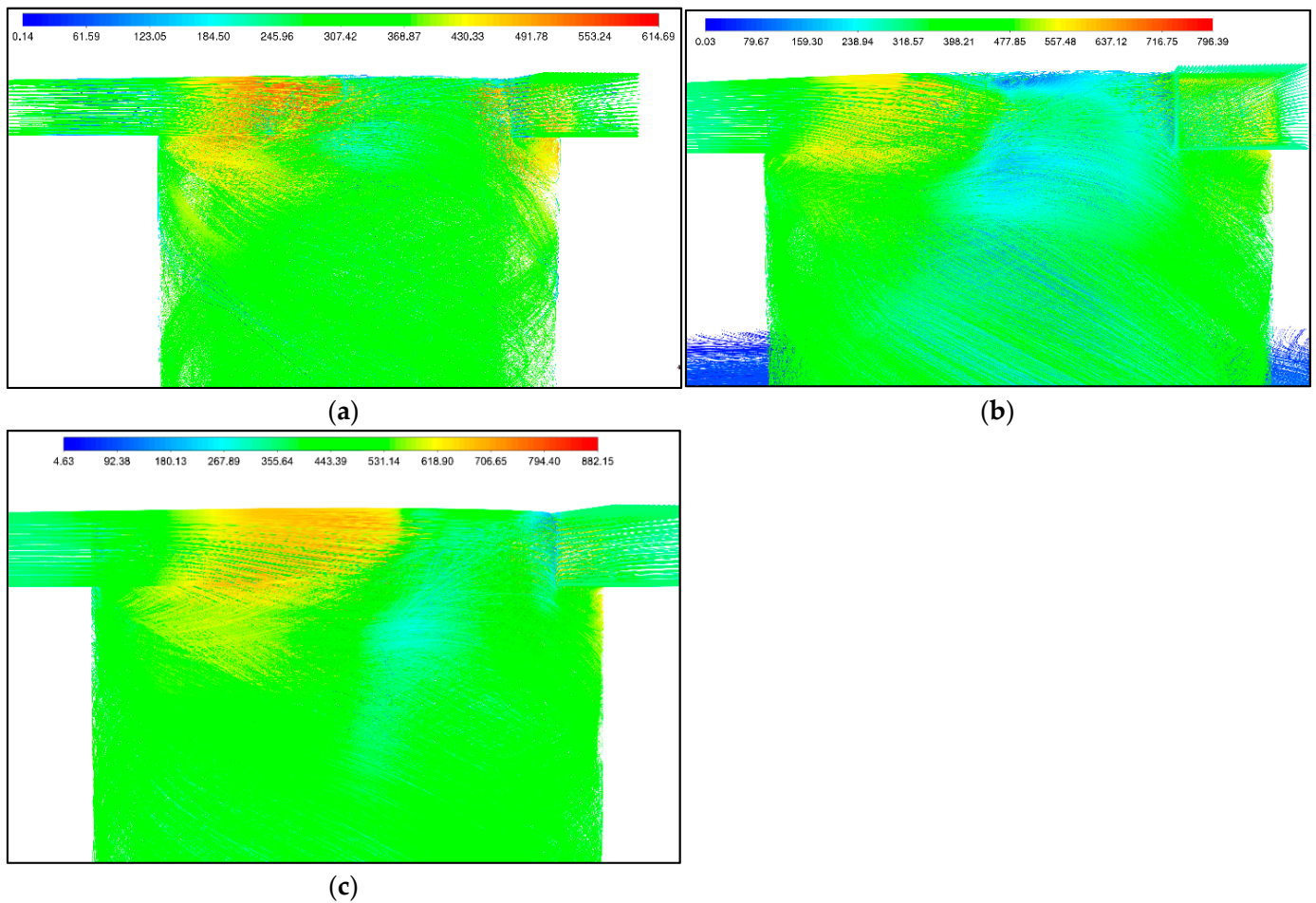


Figure 4. Velocity streamlines obtained for SVT with (a) inviscid Ar ; (b) inviscid CO_2 ; and (c) inviscid air .

3.2. SVT with the Same Geometry

As shown in Figure 6, the generated mesh satisfies the requirement y_+ for thermodynamic problems. Its value lies in the range $y_+ < 1$ for all considered gases.

The results of mesh independence analysis are presented in Table 6. As seen from Table 6, all considered grids have good agreement following the parameter GCI.

Table 6. Mesh independence study results for SVT with the same geometry.

Gas	Maximum Decreasing of Total Temperature T for Case No. 1	Maximum Decreasing of Total Temperature T for Case No. 2	Maximum Decreasing of Total Temperature T for Case No. 3	Grid Convergence Index GCI_{21} , %	Grid Convergence Index GCI_{32} , %
Ar	64.6	63.87	63.43	0.94	0.38
He	131.2	130.8	130.4	0.24	0.11
CO_2	56.1	56.3	55.8	0.39	0.67
Air	40.1	40.71	40.51	0.56	0.11

As presented in Figure 7, the flow at the periphery of the SVT is supersonic for all considered cases.

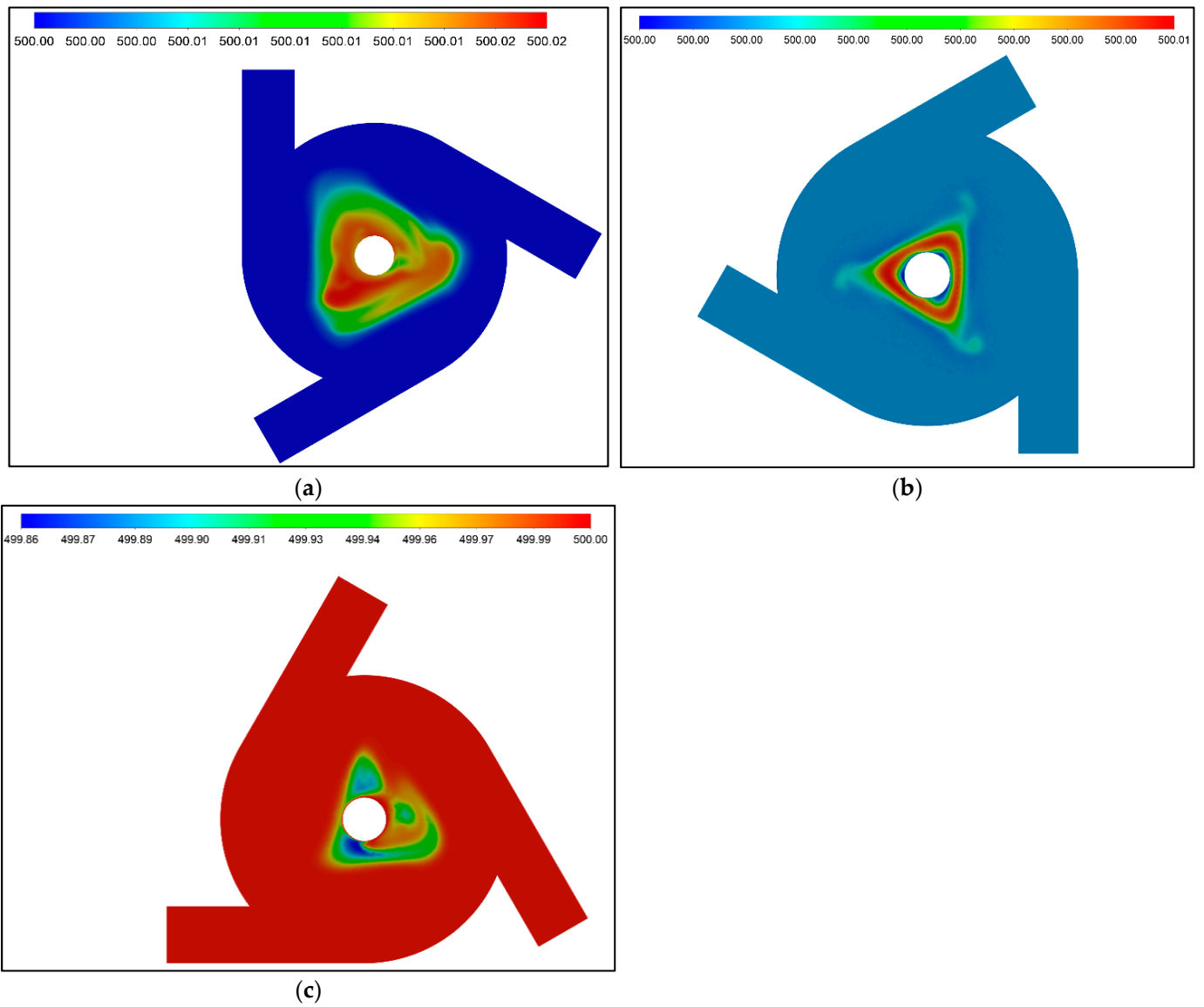


Figure 5. Total temperature contour obtained for SVT with (a) inviscid Ar; (b) inviscid CO₂; and (c) inviscid air.

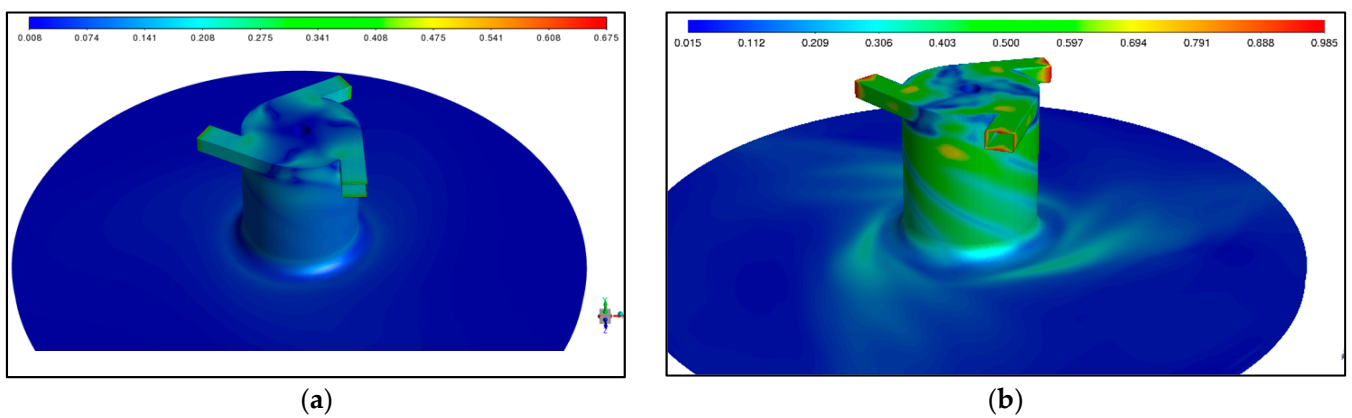


Figure 6. Cont.

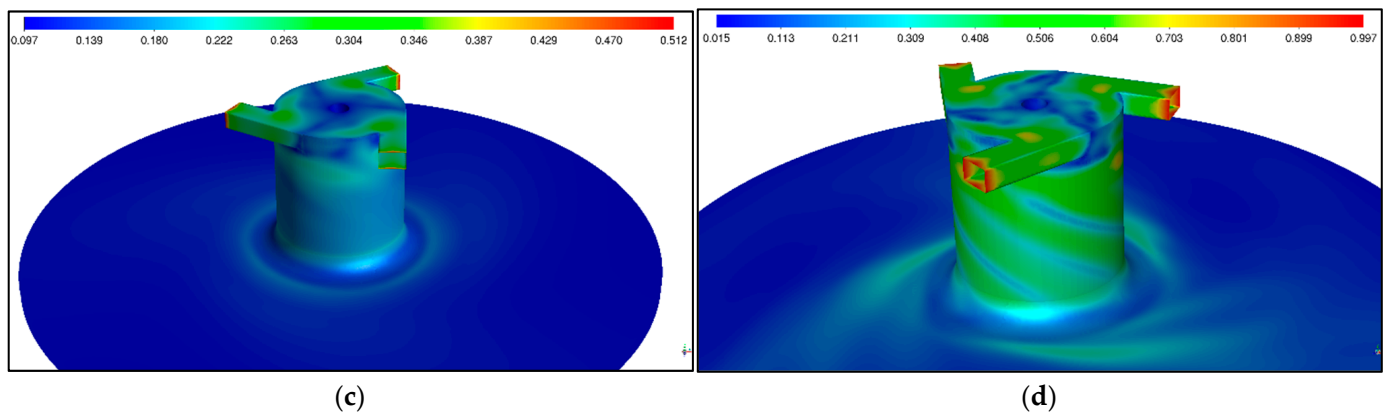


Figure 6. Contour of y_+ for SVT with (a) *Ar*; (b) *air*; (c) *He*; and (d) CO_2 .

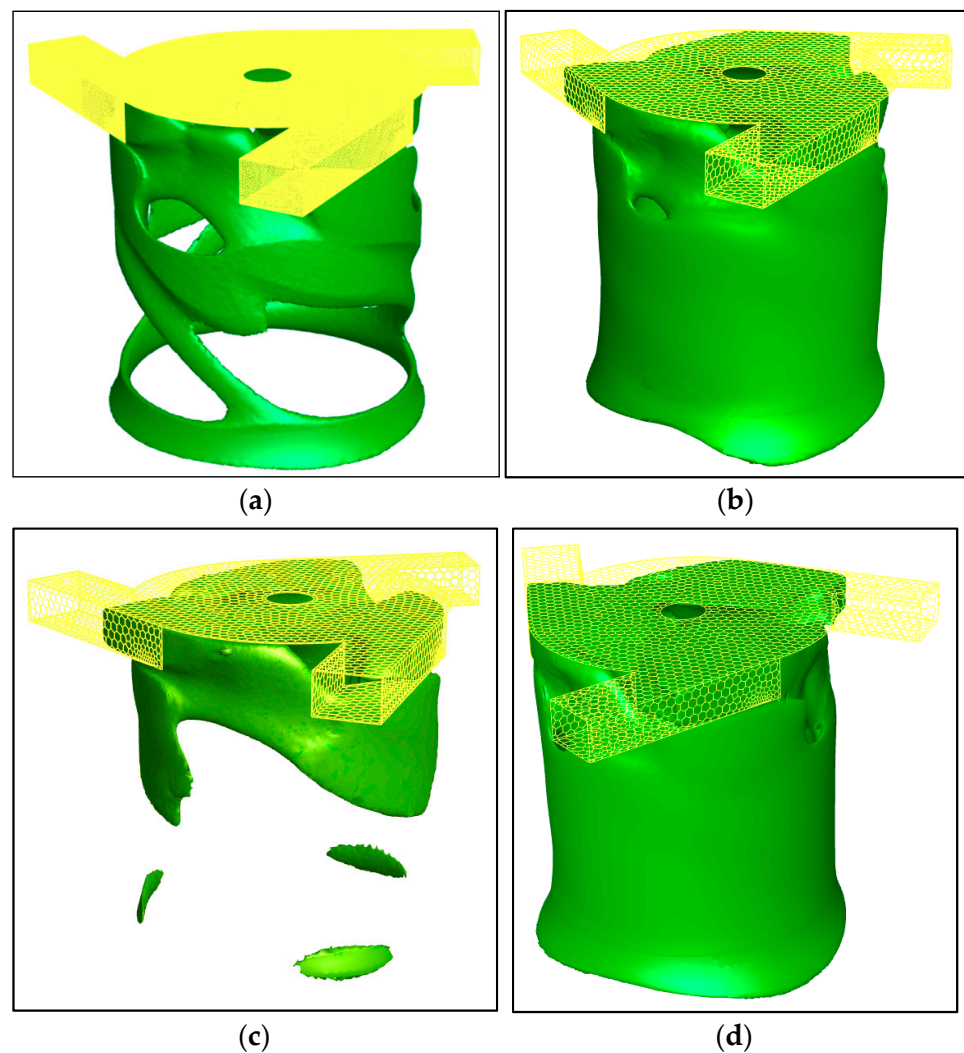


Figure 7. Mach number isosurface at $M = 1$ obtained for SVT with (a) *Ar*; (b) *air*; (c) *He*; and (d) CO_2 .

The calculation results showed that the structure of the compression shock has a similar form for all considered gases. Therefore, the contour of Mach number is shown only for SVT with *Ar*. Figure 8 clearly shows the appearance of three oblique shock waves appearing at a small distance from the nozzles.

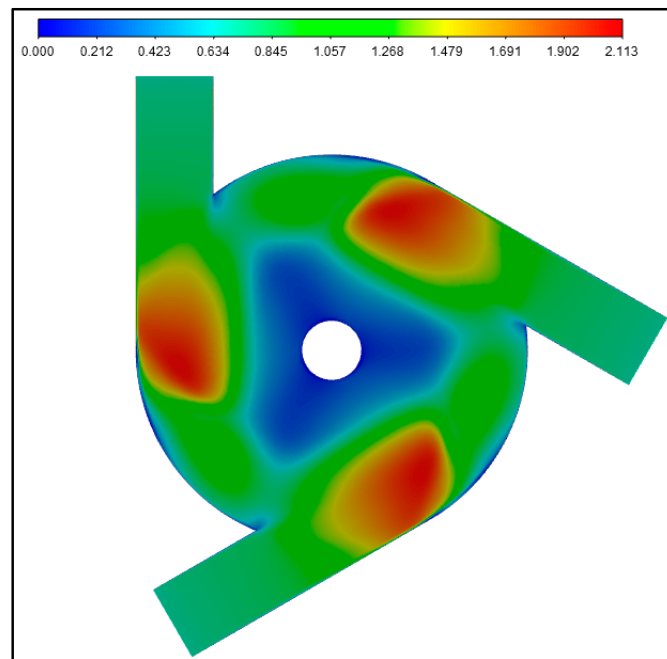


Figure 8. Countour of Mach number.

The presence of viscosity in gases led to secondary swirls, as shown in Figure 9 (indicated by a black circle). The formation of secondary swirls occurs when the gas leaves the nozzle exit of SVT. *He* and *Ar* have the most significant swirl, i.e., flow velocity around the main streamline. On the other hand, the air has the slightest degree of swirl.

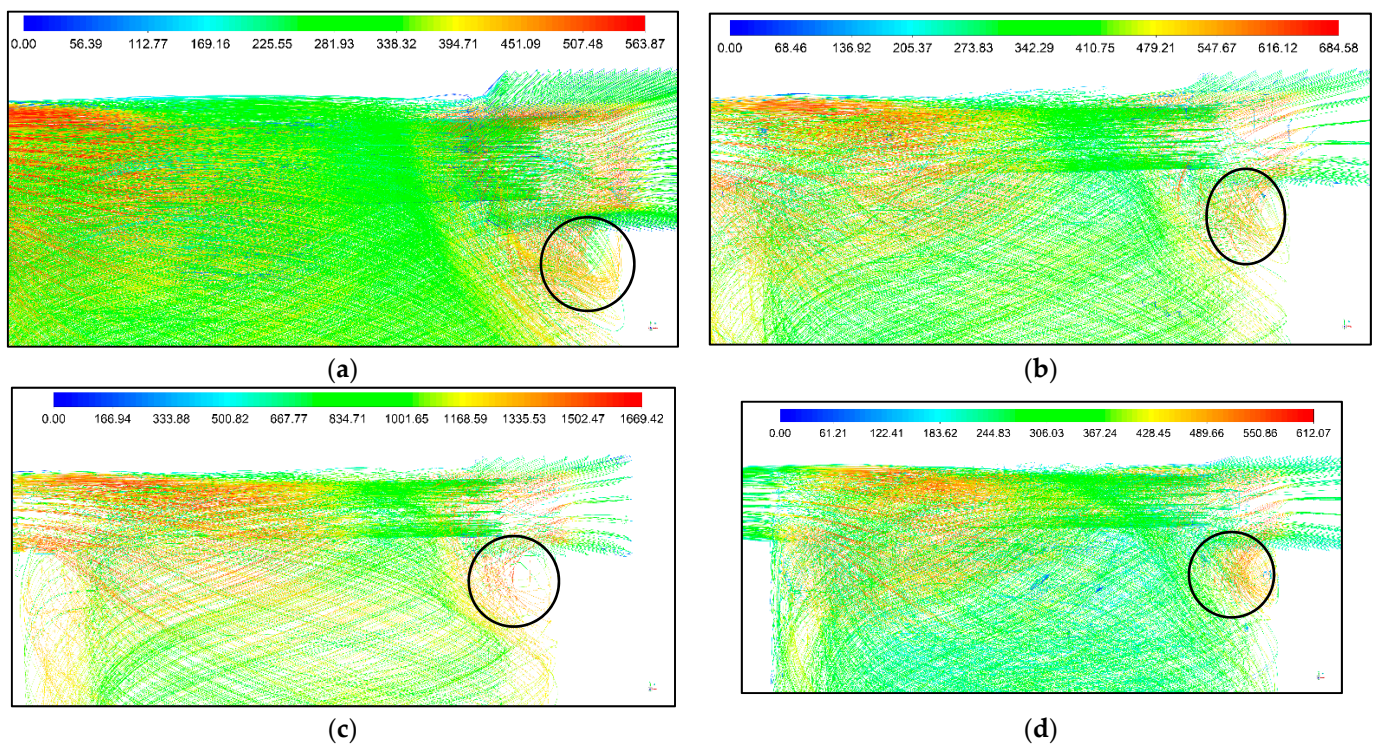


Figure 9. Velocity streamlines obtained for SVT with (a) *Ar*; (b) *air*; (c) *He*; and (d) *CO₂*.

The secondary swirl is understood as the rotation of the flow relative to its main direction (Figure 10). In Figure 10, V_s is flow velocity along the main direction (streamlines from Figure 9), and V_θ is rotation velocity relative to the main direction.

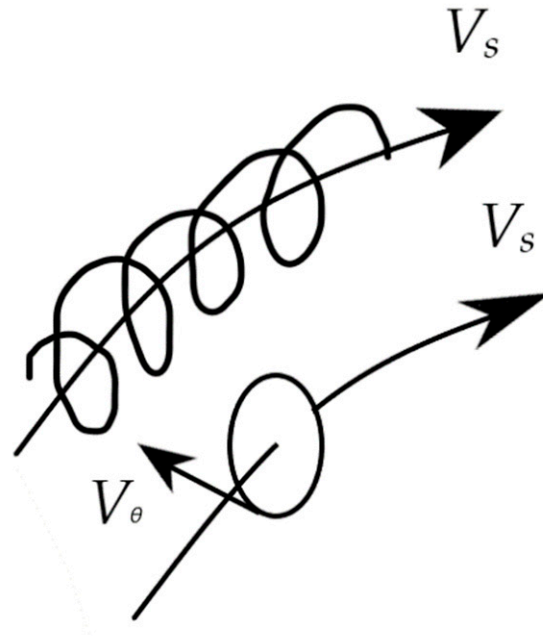


Figure 10. Scheme of secondary swirl.

SVT was dissected in the meridian direction with a step of 5 degrees (Figure 11) to determine the degree of secondary swirl and the maximum decrease in the total temperature.

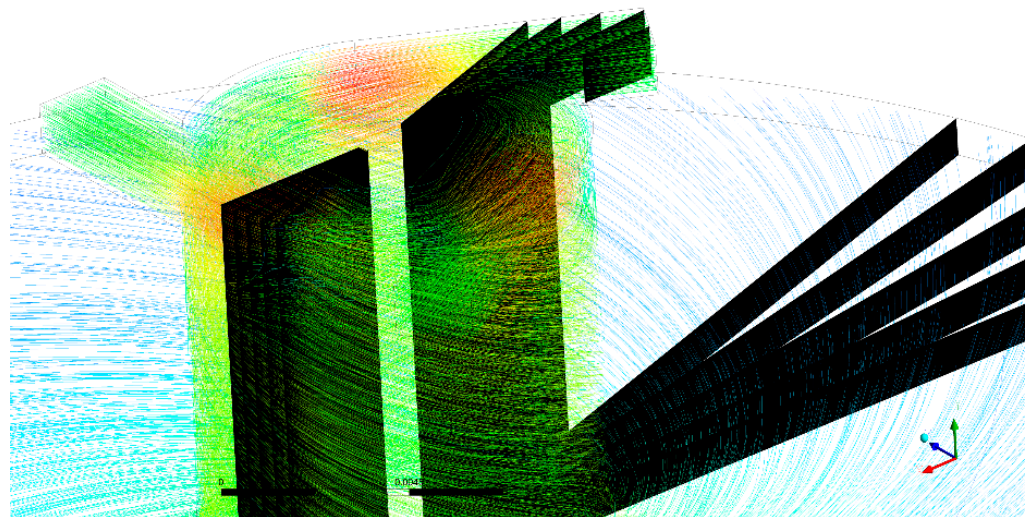


Figure 11. Cut planes SVT.

The most significant degree of flow swirling is observed at a small distance from the nozzle, as shown in Figure 12. It is also seen that the vortex has a closed structure.

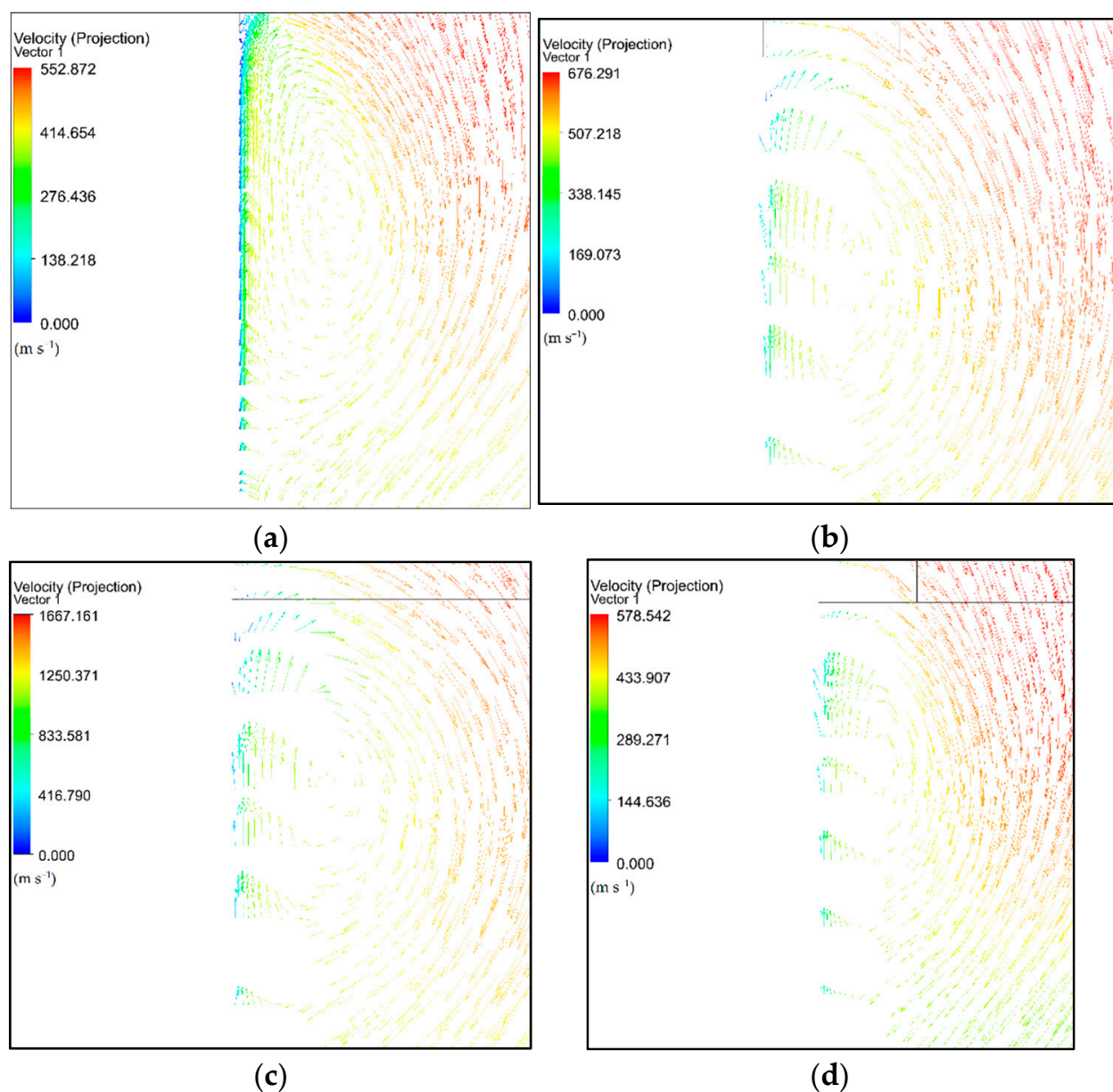


Figure 12. Vector velocity distribution obtained for SVT with (a) *Ar*; (b) *air*; (c) *He*; and (d) *CO₂*.

The results of calculating the SVT efficiency are shown in Table 7. As can be seen from Table 7, *He* has the highest cooling efficiency. On the other hand, the air has the worst efficiency. It is worth noting that *Ar* has better efficiency than *CO₂* or air, despite the lower value of the maximum possible power loss and costs.

Table 7. SVT efficiency with the same geometry.

Gas	Maximum Decreasing of Total Temperature T , K	Maximum Secondary Swirling Velocity M	Maximum Possible Power Loss and Costs ΔN , W
<i>Ar</i>	64.6	0.94	194.5
<i>He</i>	67.2	0.95	593.8
<i>CO₂</i>	45.8	0.88	209.6
<i>Air</i>	40.1	0.86	243.4

It is necessary to assess the components of power losses to analyze this result. The calculation results of power cost and loss components are presented in Figure 13. As shown

in Figure 13, *Ar* has higher power cost and loss values on the formation of secondary swirls than CO_2 and air. However, it leads to the best cooling of the flow, so it can be concluded that secondary swirls play a significant role in flow cooling. It is also worth noting that power costs and losses occur mainly due to the expansion of the flow, shock waves, and secondary swirls' formation.

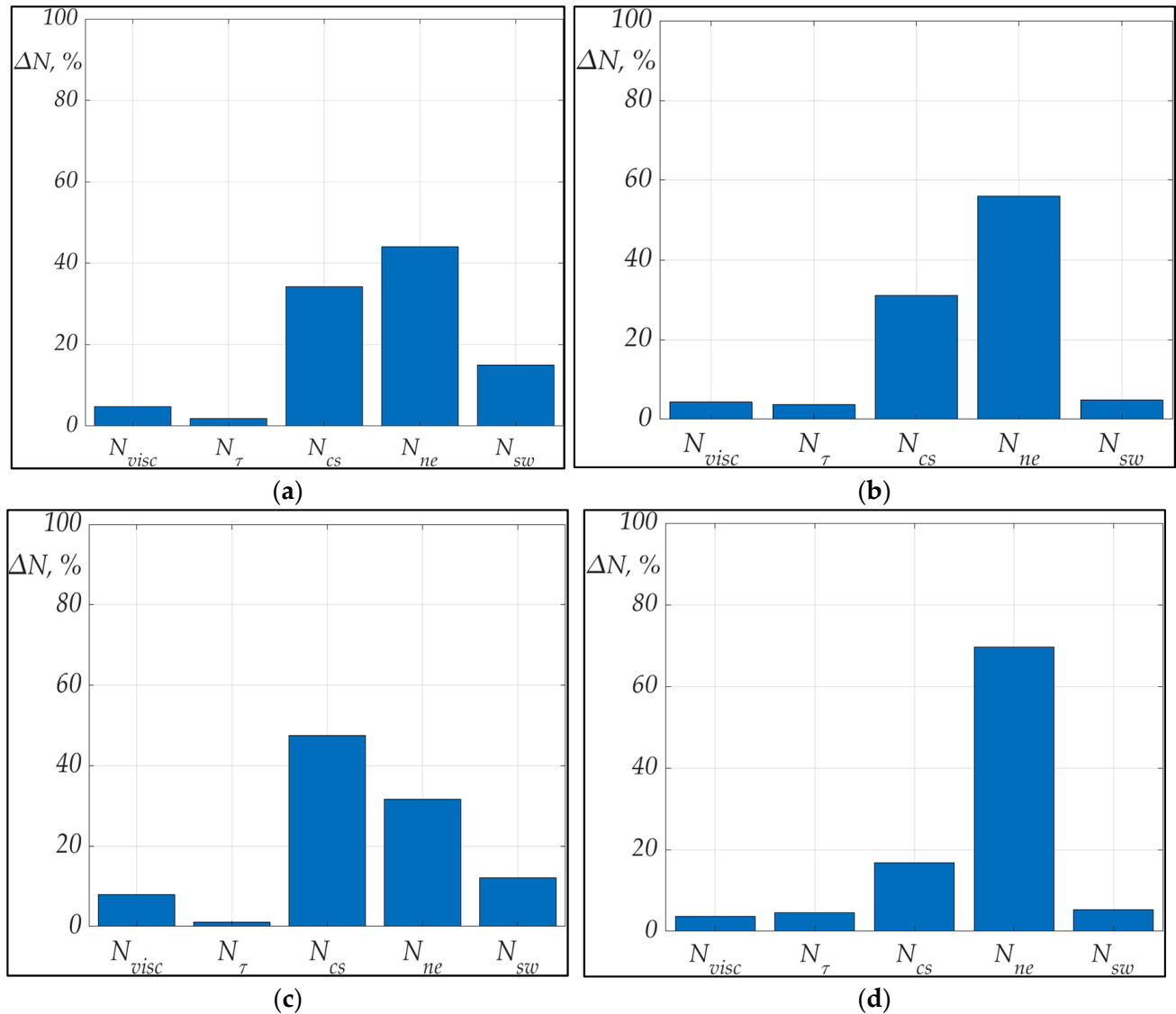


Figure 13. Power costs and losses distribution for (a) *Ar*; (b) *air*; (c) *He*; and (d) CO_2 .

3.3. SVT with the Same Reynolds Number

Figure 14 presented the contour of y_+ obtained by the calculations. It is shown that its value is less than $y_+ < 1$ and satisfies the requirement for the thermodynamic problem solution.

The mesh independence study showed a negligible effect on the control parameter (Table 8). Following the GCI parameter, its maximum value was 0.5% and was obtained for SVT with air.

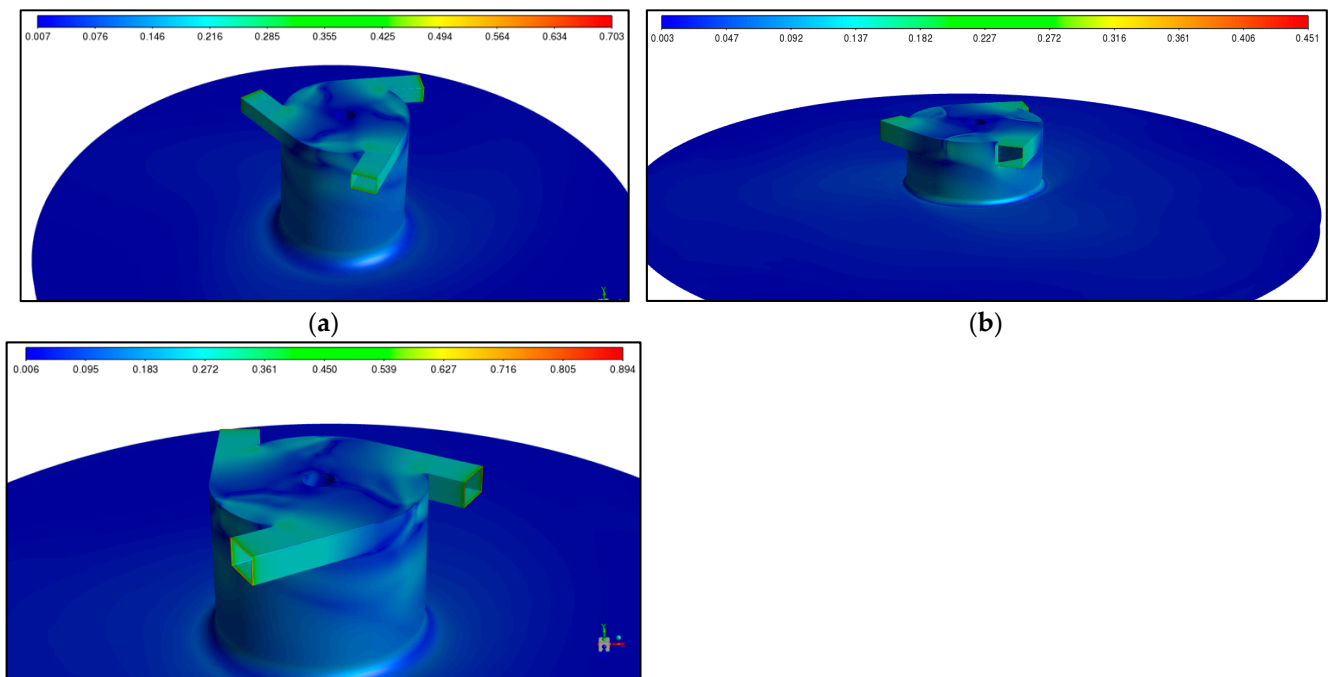


Figure 14. The contour of y_+ obtained for SVT with (a) air; (b) He; and (c) CO₂.

Table 8. Mesh independence study results for SVT with the same Reynolds number.

Gas	Maximum Decreasing of Total Temperature T for Case No. 1	Maximum Decreasing of Total Temperature T for Case No. 2	Maximum Decreasing of Total Temperature T for Case No. 3	Grid Convergence Index GCI ₂₁ , %	Grid Convergence Index GCI ₃₂ , %
He	131.2	131.08	130.7	0.06	0.17
CO ₂	56.1	55.82	55.69	0.32	0.11
Air	40.7	40.64	40.51	0.32	0.50

An increase in tube diameter led to increasing the area of supersonic flow, which is especially noticeable in SVT with helium (Figure 15).

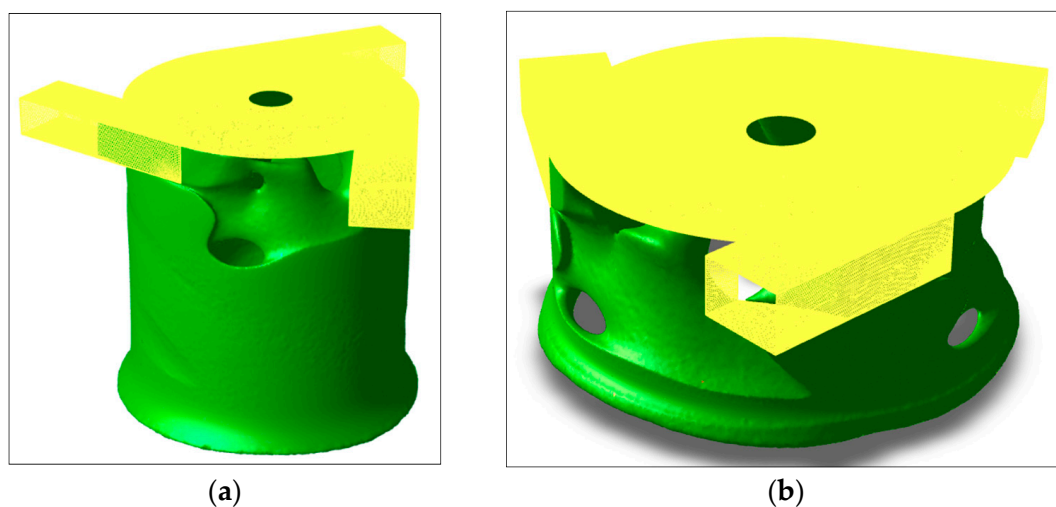
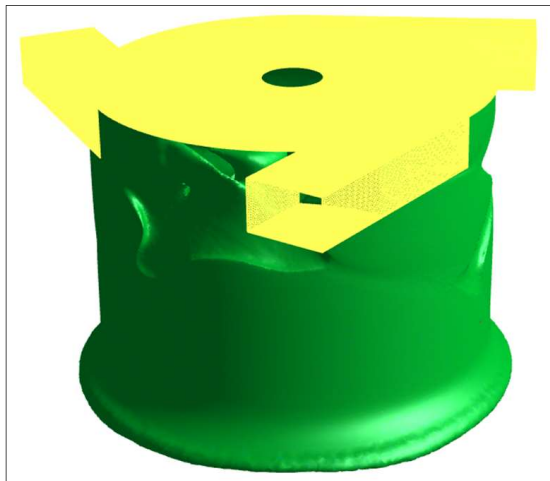


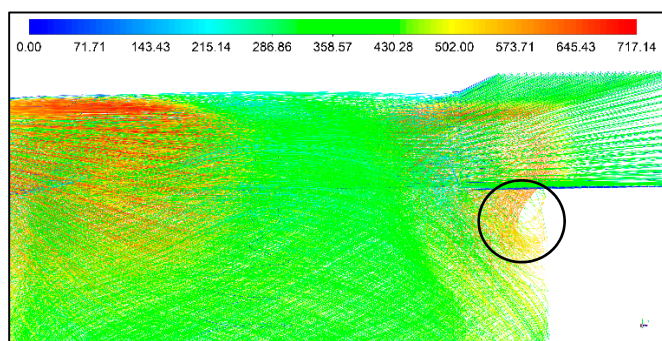
Figure 15. Cont.



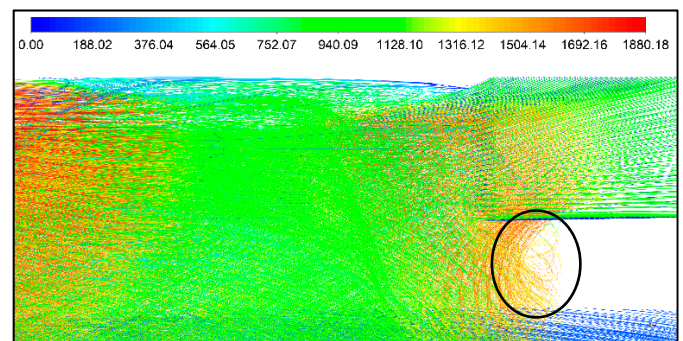
(c)

Figure 15. Mach number isosurface at $M = 1$ obtained for SVT with (a) *air*; (b) *He*; and (c) CO_2 .

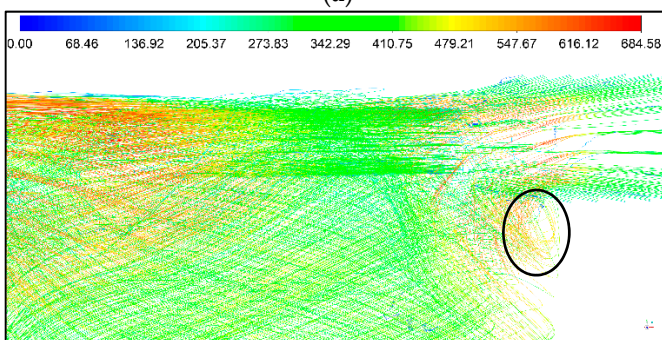
An increase in the Reynolds number changed the structure of streamlines in considered SVTs (Figure 16). It is expressed by the increase of the velocity magnitude value and the increase of swirl diameter (the right black circle in Figure 16).



(a)



(b)



(c)

Figure 16. Velocity streamlines obtained for SVT with (a) *air*; (b) *He*; and (c) CO_2 .

The changing of the vortex structure is visible in Figure 17. It has a more elongated shape in comparison to SVT of a smaller diameter. Such changes in the structure can be related to the increase of the velocity magnitude.

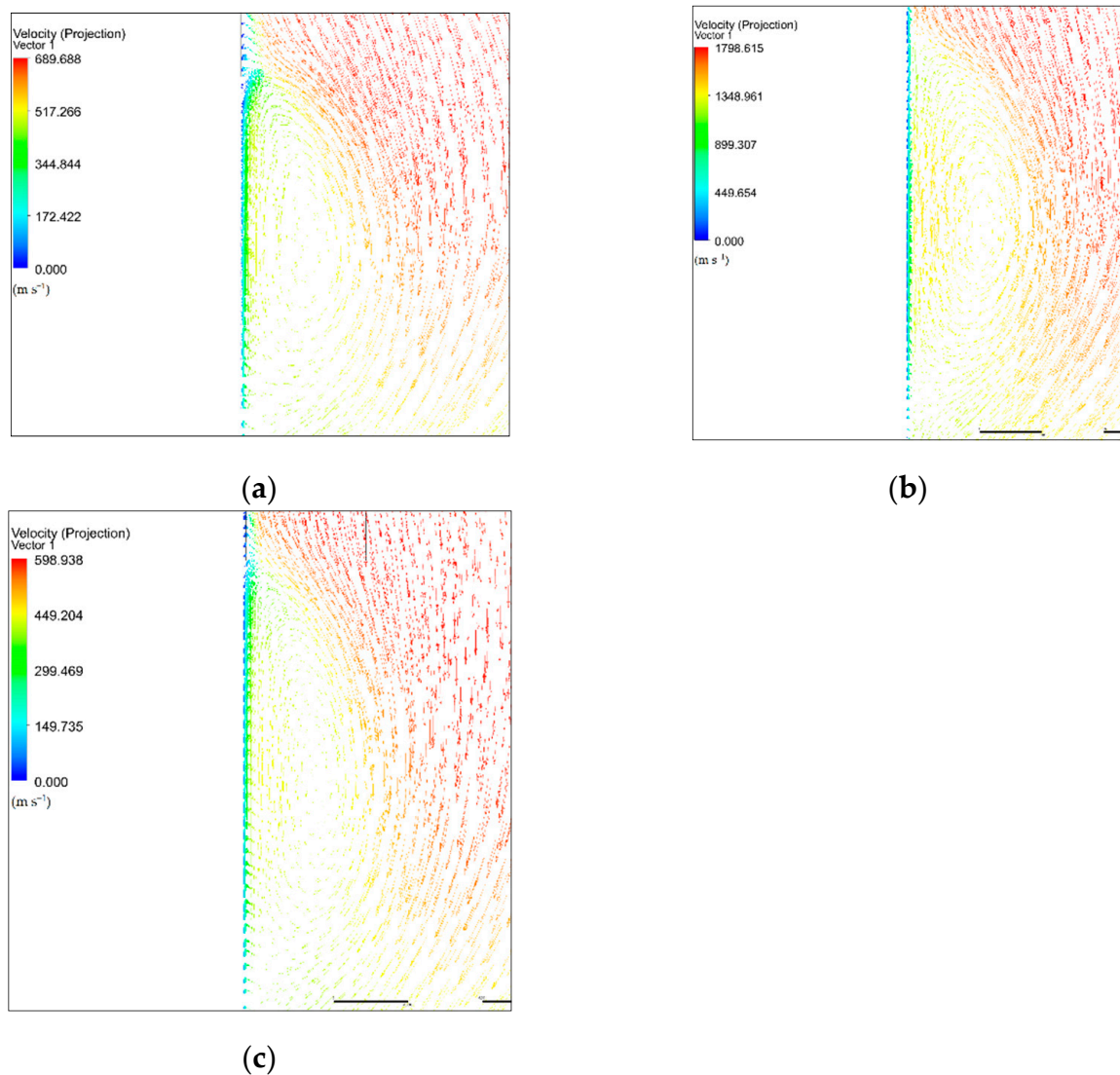


Figure 17. Vector velocity distribution obtained for SVT with (a) *air*; (b) *He*; and (c) *CO₂*.

It is expected that these changes will also lead to a noticeable change in SVT efficiency, as can be seen from Table 9. The maximum possible power loss increased significantly for SVT with helium and carbon dioxide due to the increase in mass flow rate. SVT experienced the most significant change with helium, the maximum temperature decreasing, which almost doubled. Despite the significant increase of maximum possible power loss, SVT with carbon dioxide cooling efficiency does not increase significantly.

Table 9. SVT efficiency with the same Reynolds number.

Gas	Maximum Decreasing of Total Temperature T , K	Maximum Secondary Swirling Velocity M	Maximum Possible Power Loss ΔN , W
<i>Ar</i>	64.6	0.94	194.5
<i>He</i>	131.2	0.95	8106.1
<i>CO₂</i>	56.1	0.88	741.4
<i>Air</i>	40.7	0.86	247.9

As shown in Figure 18, power cost and loss distribution for SVT with carbon dioxide did not change significantly, yet the cooling efficiency changed slightly. On the other hand, power cost and loss distribution for SVT with *He* had some changes. It is expressed by the

redistribution of losses on the expansion from the nozzle and on the compression shocks. It should also be noted that a general change in the distribution of the power losses is the decrease of losses on the viscosity and turbulence for all considered cases.

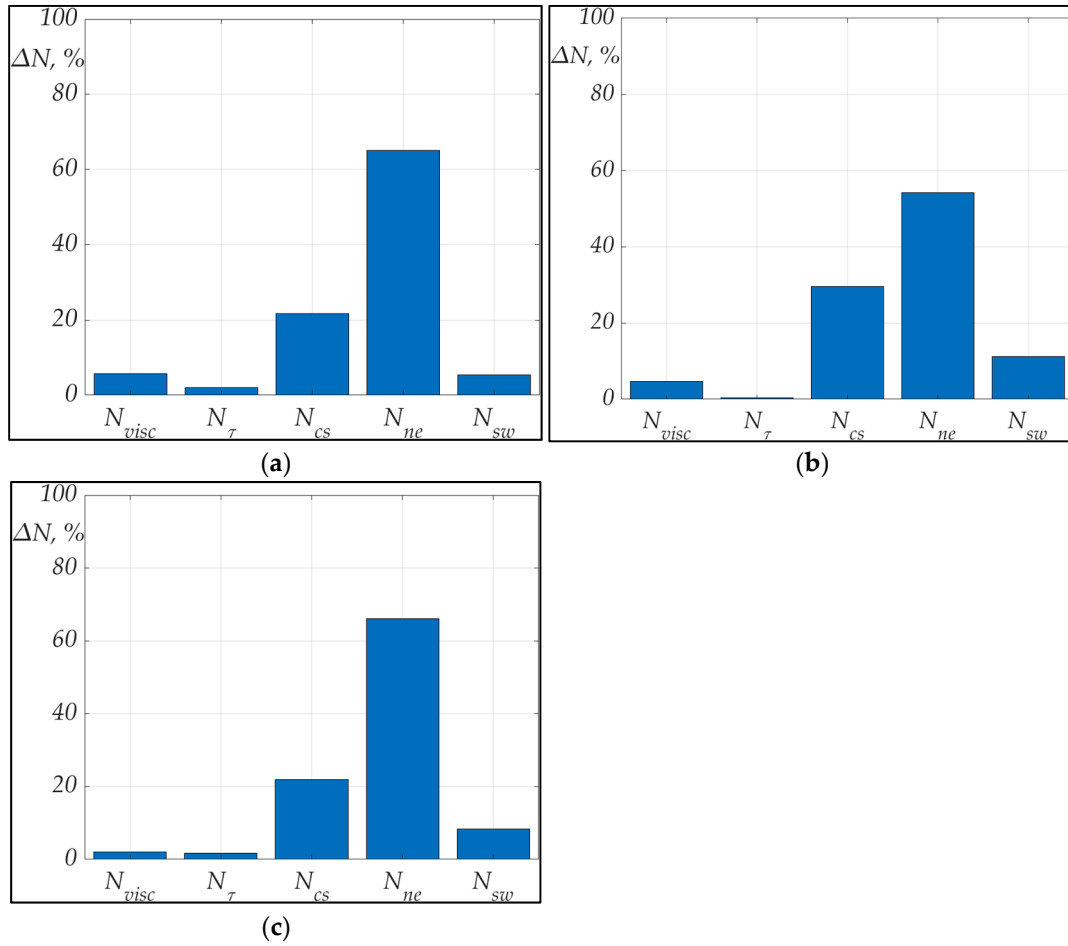


Figure 18. Power costs and losses distribution for (a) air; (b) He; and (c) CO₂.

3.4. SVT with the Same Reynolds Number and without Inner Body

The obtained value of γ_+ also satisfies the requirement of $\gamma_+ < 1$ (Figure 19) as well as in the cases of SVT with the same geometry and Reynolds numbers.

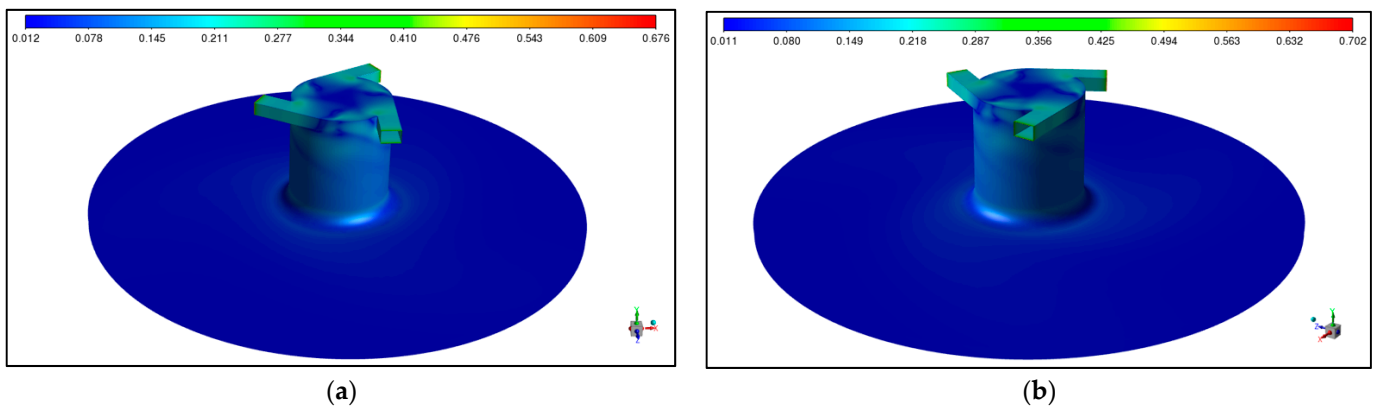


Figure 19. Cont.

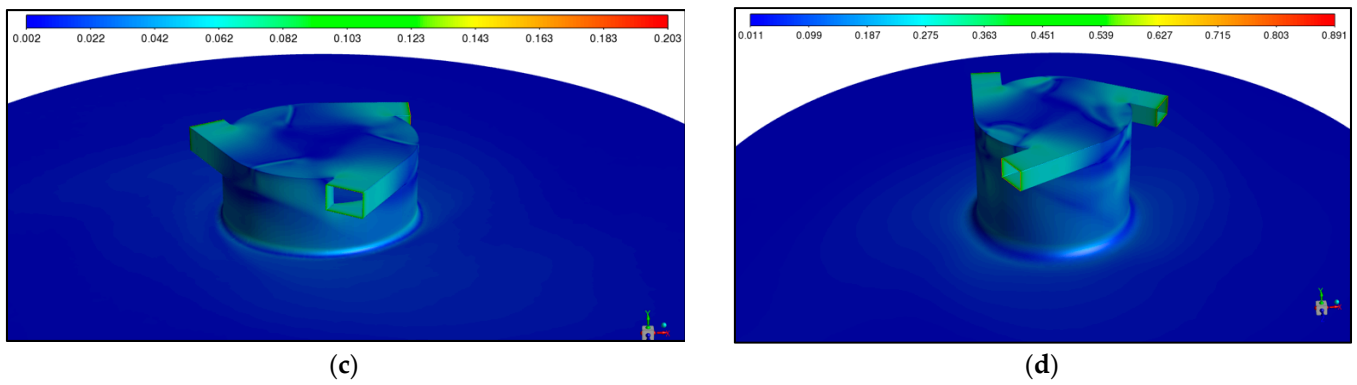


Figure 19. Contour of y_+ for SVT with (a) Ar; (b) air; (c) He; and (d) CO_2 .

Evaluation of the GCI parameter showed that the most significant discrepancy was observed for SVT with air and CO_2 (Table 10). Despite this, we can assume that its values are within the permissible range.

Table 10. SVT efficiency with the same Reynolds number and without the inner body.

Gas	Maximum Decreasing of Total Temperature T for Case No. 1	Maximum Decreasing of Total Temperature T for Case No. 2	Maximum Decreasing of Total Temperature T for Case No. 3	Grid Convergence Index GCI_{21} , %	Grid Convergence Index GCI_{32} , %
Ar	76.3	76.7	76.9	0.32	0.10
He	159.9	160.0	159.7	0.05	0.11
CO_2	57.6	57.3	56.8	0.84	1.51
Air	43.5	43.4	43.3	1.47	1.70

Similar to the SVT with the inner body, the flow at the SVT periphery is supersonic for all considered gases as well (Figure 20).

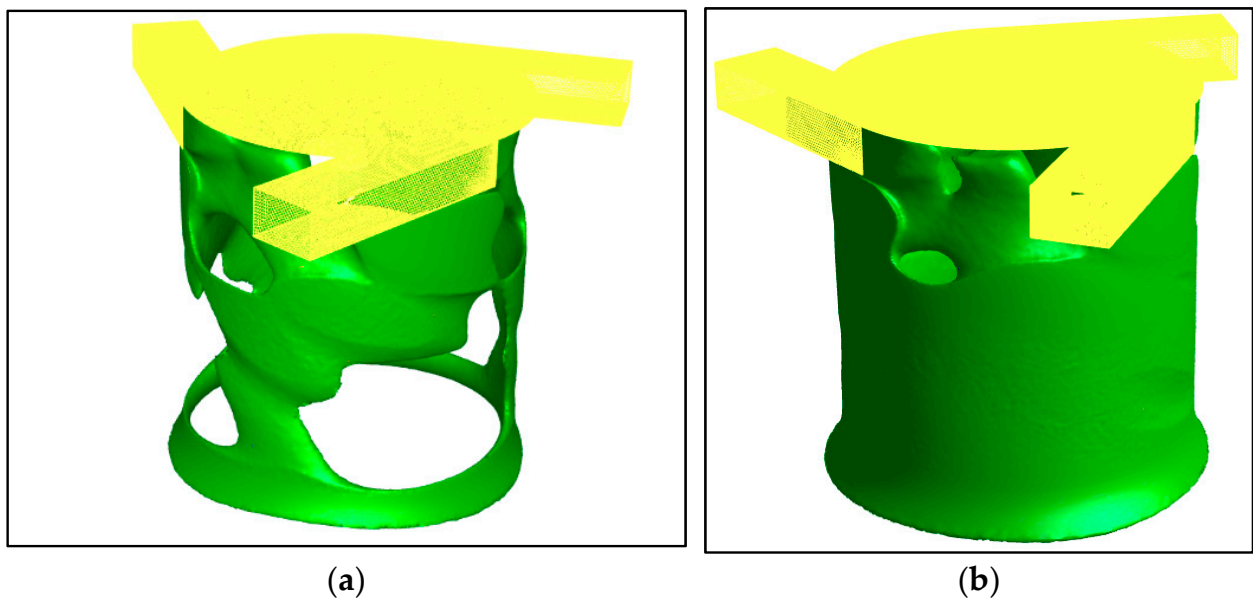


Figure 20. Cont.

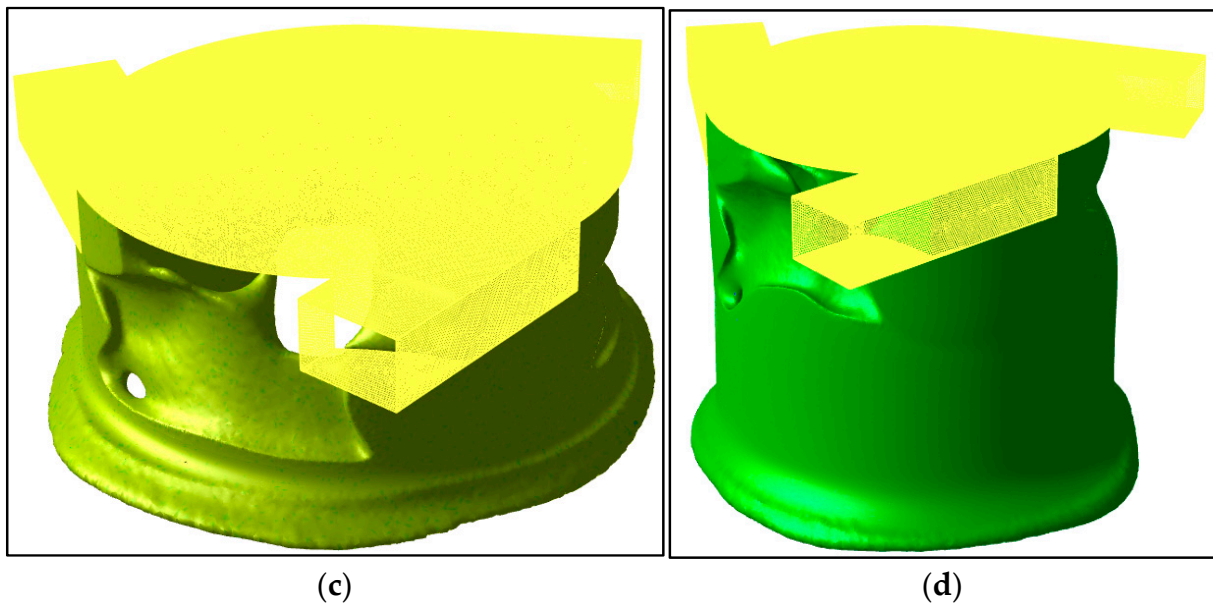


Figure 20. Mach number isosurface at $M = 1$ obtained for SVT with: (a) Ar; (b) air; (c) He; and (d) CO_2 .

Despite the similar Mach number isosurfaces, streamlines have a noticeable difference compared to SVT with the inner body (Figure 21). This is expressed by the decrease of the swirl radius (the right black circle).

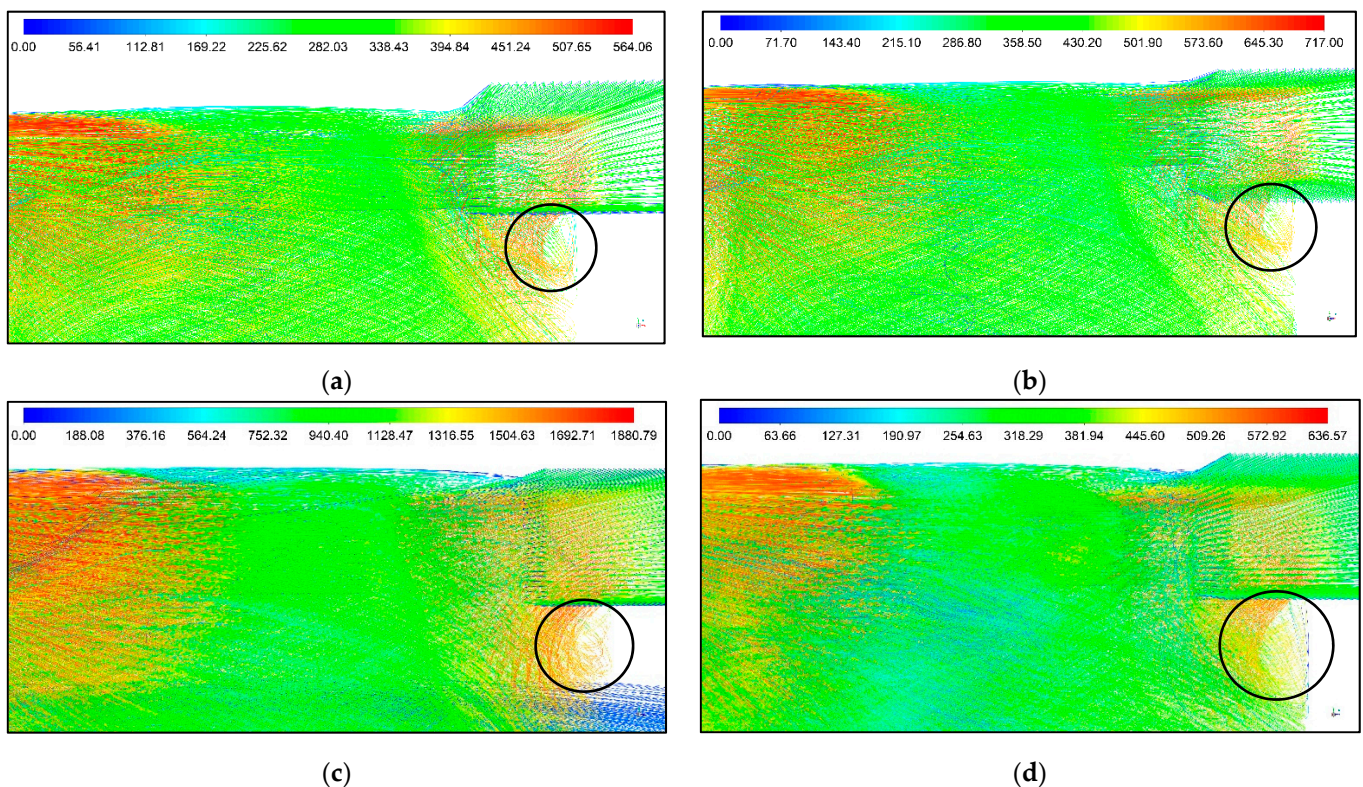


Figure 21. Velocity streamlines obtained for SVT with: (a) Ar; (b) air; (c) He; and (d) CO_2 .

The median section of a vortex also showed that its structure became less elongated than SVT with an inner body (Figure 22). The projected velocities have values close to the values for SVT with an inner body.

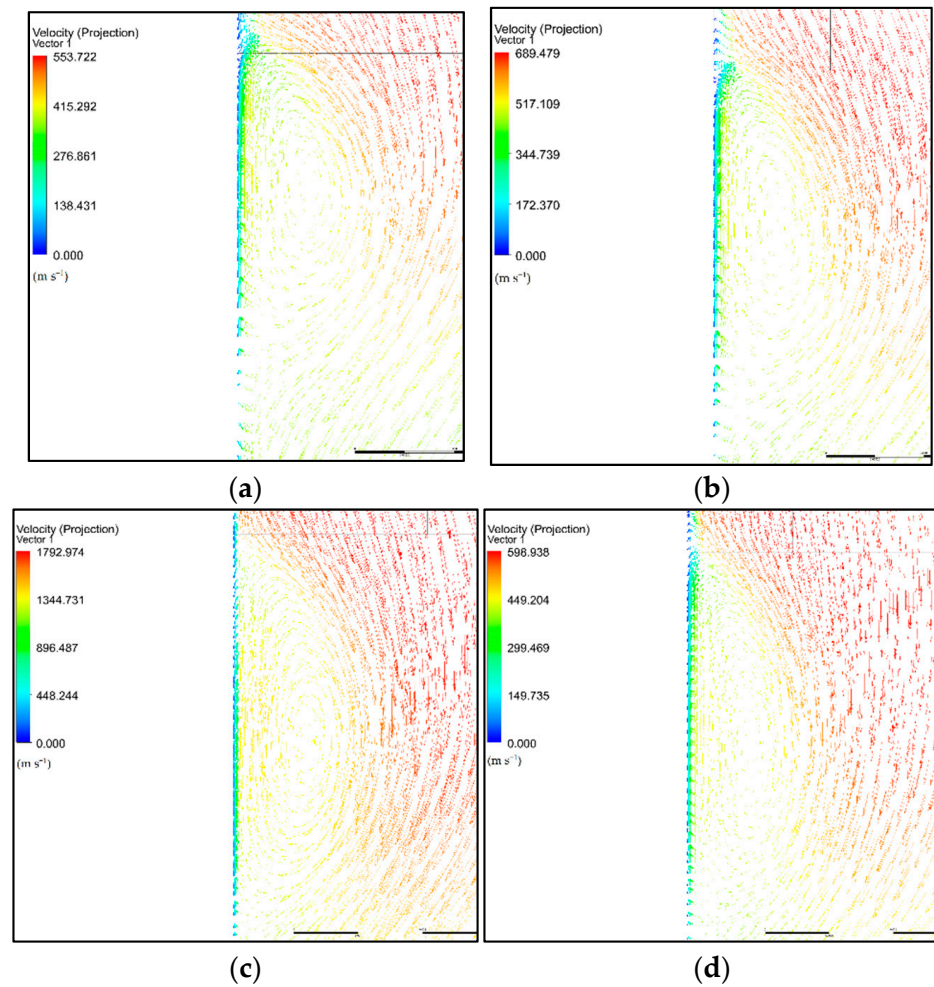


Figure 22. Vector velocity distribution obtained for SVT with: (a) *Ar*; (b) *air*; (c) *He*; and (d) *CO₂*.

Despite the similar values of projected velocities, the absence of the inner body led to an increase in SVT performance, as shown in Table 11. The resulting cooling performance for SVT with *Ar*, helium, carbon dioxide, and *air* increased by 11.7 K, 28.7 K, 1.5 K, and 2.8 K, respectively.

Table 11. SVT efficiency with the same Reynolds number and without the inner body.

Gas	Maximum Decreasing of Total Temperature T , K	Maximum Secondary Swirling Velocity M	Maximum Possible Power Loss ΔN , W
<i>Ar</i>	76.3	0.95	196.7
<i>He</i>	159.9	0.96	8263.6
<i>CO₂</i>	57.6	0.88	728.6
<i>Air</i>	43.5	0.87	271.2

A power loss analysis was carried out to establish this cause, which is shown in Figure 23. The most noticeable power loss distribution changed for helium. SVT with helium and *Ar* have the most noticeable power distribution changes, as shown in Figure 23. On the other hand, air and carbon dioxide have minor changes in power loss on the secondary swirls. This suggests that carbon dioxide and air have a slight tendency to swirl due to their thermodynamic properties. It should be noted that the power loss on the cascaded secondary swirls increased for all considered gases.

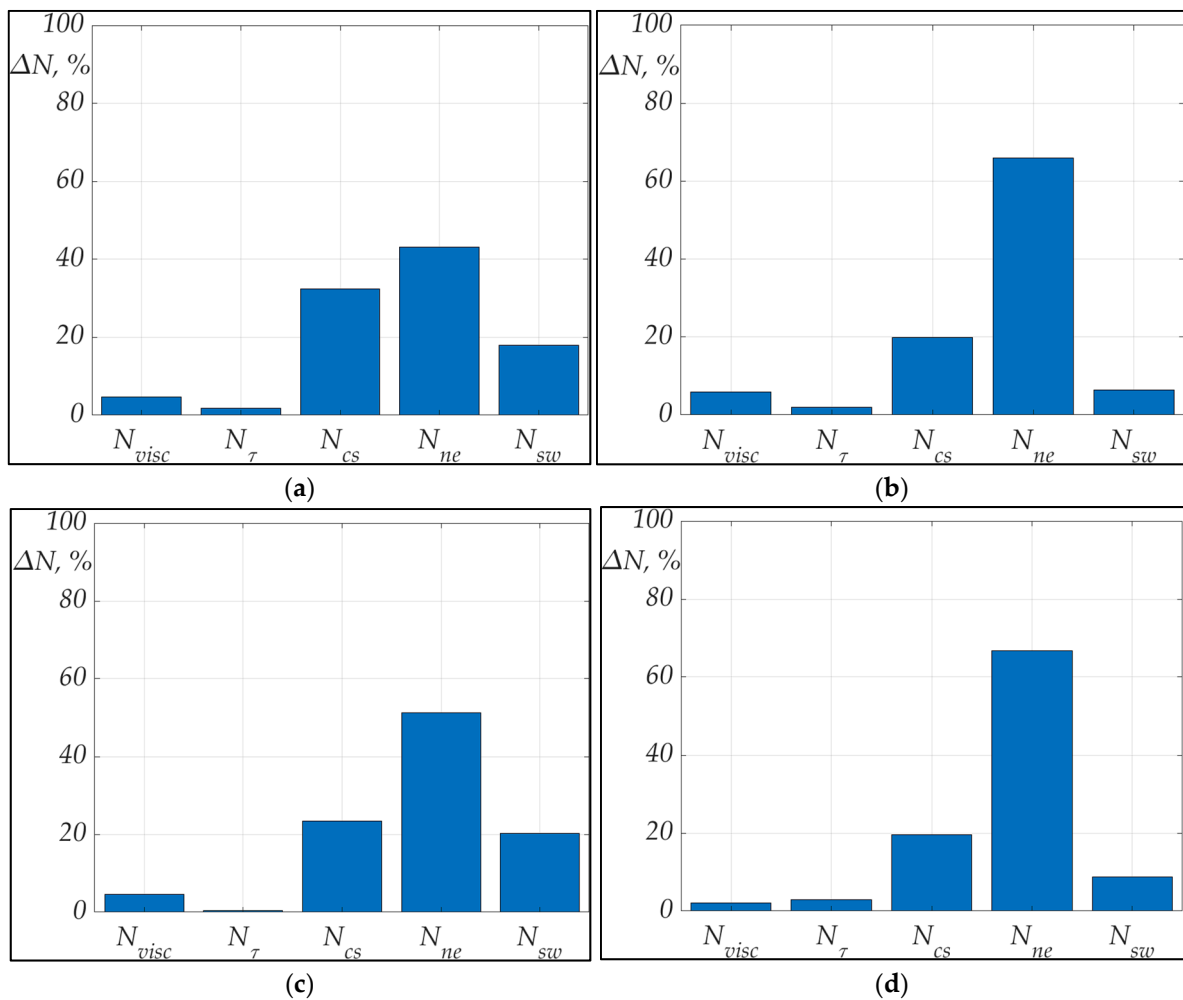


Figure 23. Power and costs losses distribution for (a) Ar; (b) air; (c) He; and (d) CO₂.

SVT with Ar was considered to analyze this phenomenon. As shown in Table 12, increasing power losses on the cascaded swirl structures decreases the remaining components. The decrease is most noticeable in power loss on the compression shocks. It can be explained that the inner body disturbs the vortex structure and decreases the cooling efficiency.

Table 12. Comparison of power losses obtained for SVT with Ar for 2 cases.

Case Number	Power Losses on the Viscosity $N_{visc}, \%$	Power Losses on the Turbulence $N_{\tau}, \%$	Power Losses on the Expansion $N_e, \%$	Power Losses on the Compression Shock $N_{cs}, \%$	Power Losses on the Cascaded Swirl Structure $N_{sw}, \%$
1	4.83	1.85	44.1	34.2	15.1
2	4.72	1.83	43.1	32.4	17.9

4. Conclusions

As results show, the secondary swirl effect is the basis for the energy separation in SVT. Indirect confirmation of the secondary swirl effect presented experimental results in the paper [49] that considered vortex glow discharge. As a conclusion, the following points can be noted:

- Kinematic viscosity plays the primary role in the formation of swirl cascaded structures which lead to the energy separation;
- It is shown that secondary swirls of the flow in SVT appeared for all considered gases of various nature;

- *He* and *Ar* have the most significant degree of swirl and, consequently, the highest separation effect;
- The presence of the inner body has led to a decrease of SVT cooling efficiency by 15%, 18%, 3%, and 6.5% for argon, helium, carbon dioxide, and air, respectively;
- Finally, a comparison of power losses obtained for argon, carbon dioxide, and air showed that the losses due to the formation of the swirl cascaded structures play the primary role in the efficiency of flow cooling.

Further research is planned to study the SVT efficiency of the energy separation processes that use the lightest and heaviest gases: hydrogen and xenon. It will also analyze the possibility of controlling the secondary swirl process and its influence on the processes of energy separation in the Ranque-Hilsch tube.

Author Contributions: Conceptualization, V.V.; Methodology, A.L.; Investigation, N.E.; Supervision V.V.; Validation, V.V.; Visualization, N.E.; writing—original draft preparation N.E. and V.V. All authors have read and agreed to the published version of the manuscript.

Funding: This research was funded by the Samara State Transport University. The publication was financially supported by the open access publication fund of the Samara State Transport University.

Acknowledgments: The authors would like to thank the president of Samara State Transport University M.A. Garanin for the donation to publish this paper.

Conflicts of Interest: The authors declare no conflict of interest.

References

1. Ranque, G.J. Experiments on Expansions in a Vortex with Simultaneous Exhaust of Hot and Cold Air. *Phys. Radium* **1933**, *4*, 112–114.
2. Hilsch, R. The Use of the Expansion of Gases in a Centrifugal Field as Cooling Process. *Rev. Sci. Instrum.* **1947**, *18*, 108–113. [[CrossRef](#)] [[PubMed](#)]
3. Scheper, G.S. The vortex tube-internal flow data and a heat transfer theory. *Refrig. Eng.* **1951**, *59*, 985–989.
4. Fulton, C.D. Ranque's tube. *ASHRAE J.* **1950**, *58*, 473–479.
5. Van Deemter, J.J. On the theory of the Ranque-Hilsch cooling effect. *Appl. Sci. Res.* **1952**, *3*, 174–196. [[CrossRef](#)]
6. Deissler, R.G.; Perlmutter, M. Analysis of the flow and energy separation in a turbulent vortex. *Int. J. Heat Mass Transf.* **1960**, *1*, 173–191. [[CrossRef](#)]
7. Reynolds, A.J. Energy flows in a vortex tube. *Z. Angew. Math. Phys.* **1961**, *12*, 343–357. [[CrossRef](#)]
8. Holman, J.P.; Moore, G.D. An experimental study of vortex chamber flow. *J. Basic. Eng.* **1961**, *83*, 632–636. [[CrossRef](#)]
9. Parulekar, B.B. Performance of short vortex tube. *J. Refrig.* **1961**, *6*, 74–80.
10. Merkulov, A.P.; Kolyshchev, N.D. The investigation of the temperature fields into vortex tube with the diffuser. *Proc. Kuibyshev Aviat. Inst.* **1965**, *22*, 81–89. (In Russian)
11. Merkulov, A.P. *The Vortex Effect and Its Application in Technology*, 1st ed.; Mashinostroyeniye: Moscow, Russia, 1969. (In Russian)
12. Hinze, J.O. *Turbulence*, 2nd ed.; McGraw-Hill College: New York, NY, USA, 1975.
13. Celik, A.; Yilaz, M.; Yildiz, O.F. Effects of vortex tube on exhaust emissions during cold start of diesel engines. *Appl. Energy Combust. Sci.* **2021**, *6*, 100027. [[CrossRef](#)]
14. Celik, A.; Yilaz, M.; Yildiz, O.F. Improvement of diesel engine startability under low temperatures by vortex tubes. *Energy Rep.* **2019**, *6*, 17–27. [[CrossRef](#)]
15. Chen, J.; Gao, X.; Shao, S.; Hu, H.; Xie, J.; Li, N.; Gao, N. Numerical investigation of the vortex tube performance in novel precooling methods in the hydrogen fueling station. *Int. J. Hydrog. Energy* **2021**, *46*, 5548–5555. [[CrossRef](#)]
16. Maestre-Cambronel, D.; Barros, J.G.; Gonzalez-Quiroga, A.; Bula, A.; Duarte-Forero, J.; Sustain, J. Thermoeconomic analysis of improved exhaust waste heat recovery system for natural gas engine based on Vortex Tube heat booster and supercritical CO₂ Brayton cycle. *Energy Technol. Assess.* **2021**, *47*, 101355. [[CrossRef](#)]
17. Shmroukh, A.N.; Attalla, M.; Abd El-Naser Abd El-Hakim, A. Experimental investigation of a novel sea water desalination system using Ranque-Hilsch vortex tube. *Appl. Therm. Eng.* **2019**, *149*, 658–664. [[CrossRef](#)]
18. Zhang, B.; Guo, X. Prospective applications of Ranque-Hilsch vortex tubes to sustainable energy utilization and energy efficiency improvement with energy and mass separation. *Renew. Sustain. Energy Rev.* **2018**, *89*, 135–150. [[CrossRef](#)]
19. Nash, J.M. The Ranque-Hilsch vortex tube and its application to spacecraft environmental control systems. *Dev. Theor. Appl. Mech.* **1972**, *6*, 35–90.
20. Matveev, K.I.; Leachman, J. Numerical investigation of vortex tubes with extended vortex chambers. *Int. J. Refrig.* **2019**, *108*, 145–153. [[CrossRef](#)]

21. Qyyum, M.A.; Noon, A.A.; Wei, F.; Lee, M. Vortex tube shape optimization for hot control valves through computational fluid dynamics. *Int. J. Refrig.* **2019**, *102*, 151–158. [[CrossRef](#)]
22. Guo, X.; Zhang, B. Analysis of the unsteady heat and mass transfer processes in a Ranque-Hilsch vortex tube: Tube optimization criteria. *Int. J. Heat Mass Transf.* **2018**, *127*, 68–79. [[CrossRef](#)]
23. Liang, F.; Tang, G.; Xu, C.; Wang, C.; Wang, Z.; Wang, J.; Li, N. Experimental investigation on improving the energy separation efficiency of vortex tube by optimizing the structure of vortex generator. *Appl. Therm. Eng.* **2021**, *195*, 117222. [[CrossRef](#)]
24. Pourmahmoud, N.; Hassanzadeh, A.; Moutaby, O. Numerical analysis of the effect of helical nozzles gap on the cooling capacity of Ranque-Hilsch vortex tube. *Int. J. Refrig.* **2012**, *35*, 1473–1483. [[CrossRef](#)]
25. Avci, M. The effects of nozzle aspect ratio and nozzle number on the performance of the Ranque-Hilsch vortex tube. *Appl. Therm. Eng.* **2013**, *50*, 302–308. [[CrossRef](#)]
26. Rafiee, S.E.; Sadeghiazad, M.M. Experimental analysis on impact of navigator's angle on velocimetry and thermal capability of RH-vortex tube. *Appl. Therm. Eng.* **2020**, *169*, 114907. [[CrossRef](#)]
27. Guo, X.; Liu, B.; Lv, J.; Zhang, B.; Shan, Y. An optimization method on managing Ranque-Hilsch vortex tube with the synergy between flow structure and performance. *Int. J. Refrig.* **2021**, *126*, 123–132. [[CrossRef](#)]
28. Xue, Y.; Arjomandi, M.; Kelso, R. Energy analysis within a vortex tube. *Exp. Therm. Fluid Sci.* **2014**, *52*, 139–145. [[CrossRef](#)]
29. Liang, F.; Wang, H.; Tang, G. Temperature separation characteristics of CH₄-CO₂ binary gas mixture within a vortex tube. *Int. J. Therm. Sci.* **2021**, *16*, 106726. [[CrossRef](#)]
30. Aghagoli, A.; Sorin, M. Thermodynamic performance of a CO₂ vortex tube based on 3D CFD flow analysis. *Int. J. Refrig.* **2019**, *108*, 124–137. [[CrossRef](#)]
31. Chen, J.; Zeng, R.; Zhang, W.; Qiu, L.; Zhang, X. Numerical analysis of energy separation in Ranque-Hilsch vortex tube with gaseous hydrogen using real gas model. *Appl. Therm. Eng.* **2018**, *140*, 287–294. [[CrossRef](#)]
32. Volov, V.; Lyaskin, A. Effect of secondary swirl in supersonic gas and plasma flows in the self-vacuuming vortex tube. In Proceedings of the MATEC of Web of Conferences, International Conference on Combustion Physics and Chemistry, Samara, Russia, 24–28 July 2018; Volume 208, p. 20.
33. Volov, V.; Lyaskin, A. Investigation of the cascade mechanism of energy exchange in swirling gas flows based on the effect of secondary swirling. *J. Phys. Conf. Ser.* **2020**, *1677*, 012032. [[CrossRef](#)]
34. Vitovsky, O.V. Experimental study of energy separation in a Ranque-Hilsch tube with a screw vortex generator. *Int. J. Refrig.* **2021**, *126*, 272–279. [[CrossRef](#)]
35. Hamdan, M.O.; Al-Omari, S.-A.B.; Oweimer, A.S. Experimental study of vortex tube energy separation under different tube design. *Exp. Therm. Fluid Sci.* **2018**, *91*, 306–311. [[CrossRef](#)]
36. Guo, X.; Zhang, B.; Shan, Y. Analysis on the patterns of precessing frequency characteristics and energy separation processes in a Ranque-Hilsch vortex tube. *Int. J. Therm. Sci.* **2021**, *168*, 107067. [[CrossRef](#)]
37. Guo, X.; Zhang, B.; Shan, Y. LES study on the working mechanism of large-scale precessing vortices and energy separation process of Ranque-Hilsch vortex tube. *Int. J. Therm. Sci.* **2021**, *163*, 106818. [[CrossRef](#)]
38. Guo, X.; Zhang, B. Computational investigation of precessing vortex breakdown and energy separation in a Ranque-Hilsch vortex tube. *Int. J. Refrig.* **2018**, *85*, 42–57. [[CrossRef](#)]
39. Kirmaci, V.; Kaya, H.; Celebi, I. An experimental and exergy analysis of a thermal performance of a counter flow Ranque-Hilsch vortex tube with different nozzle materials. *Int. J. Refrig.* **2018**, *85*, 240–254. [[CrossRef](#)]
40. Kaya, H.; Gunver, F.; Kirmaci, V. Experimental investigation of thermal performance of parallel connected vortex tubes with various nozzle materials. *Appl. Therm. Eng.* **2018**, *136*, 287–292. [[CrossRef](#)]
41. Menter, F.R. Two-equation eddy-viscosity turbulence models for engineering application. *AIAA J.* **1994**, *32*, 1598–1605. [[CrossRef](#)]
42. Andersson, B.; Andersson, R. *Computational Fluid Dynamics for Engineers*, 1st ed.; Cambridge University Press: Cambridge, UK, 2012; p. 97.
43. Pettersson Rief, B.A.; Andersson, H.I. Prediction of turbulence-generated secondary mean flow in a square duct. *Flow Turbul. Combust.* **2002**, *68*, 41–61. [[CrossRef](#)]
44. Volov, V.T. Limit energy theorem for gas flow systems. *J. Eng. Thermophys.* **2018**, *27*, 489–500. [[CrossRef](#)]
45. Abramovich, G.N. *Applied Gas Dynamics*, 3rd ed.; Ft. Belvoir Defense Technical Information Center: Washington, CA, USA, 1973.
46. Poling, B.E.; Thomson, G.H.; Friend, D.G.; Rowley, R.L.; Wilding, W.V. *Perry's Chemical Engineers. Handbook*, 8th ed.; McGraw-Hill Companies: New York, NY, USA, 2008.
47. Richardson, L.F. The approximate arithmetical solution by finite differences of physical problems involving differential equations, with an application to the stresses in a masonry dam. *Philos. Trans. R. Soc. A* **1911**, *210*, 307–357.
48. Schwer, L.E. Is your mesh refined enough? Estimating discretization error using GCI. In Proceedings of the LS-DYNA Anwenderforum, Bamberg, Germany, 30 September–1 October 2008; Franz, U., Ed.; DYNAmore GmbH: Stuttgart, Germany, 2008; Volume 1, pp. 45–54.
49. Volov, V.T.; Lamazhapov, K.D.; Margolin, A.D.; Mishchenko, A.V.; Shmelev, V.M. Vortex glow discharge theory and ways of creating a CO₂ laser on its basis. The vortex effect and its application in technology. In Proceedings of the 5th All-Union Scientific and Technical Conference, Kuybyshev, Russia, 13–17 June 1988.